catalysts

MDPI

Article

The Role of Titanium Species in Ti-SBA-15 Materials for the UV–Photocatalytic Degradation of Acetaminophen in Water

Juan Pablo Chávez-León [1], Mariana Lizeth López-García [1], Uriel Caudillo-Flores [2], Dora A. Solis-Casados [3], Jaime Espino-Valencia [1,*], Deysi Amado-Piña [3] and Horacio González [1,*]

[1] Facultad de Ingeniería Química, Universidad Michoacana de San Nicolás de Hidalgo, Morelia 58060, Mexico; 1419420f@umich.mx (J.P.C.-L.); 1901736x@umich.mx (M.L.L.-G.)
[2] Centro de Nanociencias y Nanotecnología, Universidad Nacional Autónoma de México, Ensenada 22800, Mexico; ucaudillo@ens.cnyn.unam.mx
[3] Facultad de Química, Centro Conjunto de Investigación en Química Sustentable, Universidad Autónoma del Estado de México, Toluca 50120, Mexico; dasolisc@uaemex.mx (D.A.S.-C.); damadop_ext@uaemex.mx (D.A.-P.)
* Correspondence: jaime.espino@umich.mx (J.E.-V.); horacio.gonzalez@umich.mx (H.G.)

Abstract

Water contamination by acetaminophen, a compound difficult to remove via conventional treatments, has become a growing environmental concern due to its excessive consumption in recent years. Among emerging methods for removing this pollutant, heterogeneous photocatalysis is a promising option that enables catalyst recovery and reuse. In this research, Ti-SBA-15 materials with different Si/Ti molar ratios were synthesized by a one-step sol–gel method to improve Ti dispersion within the SBA-15 silica framework. A detailed characterization of the materials was carried out using XRD, SEM, ICP-OES, N_2 physisorption, UV-Vis-DRS, XPS, and zeta potential techniques. The results showed that the characteristic hexagonal mesoporous structure of SBA-15 was largely preserved at high Si/Ti ratios, while ICP-OES analysis showed that the synthesis method allowed Ti incorporation close to the theoretical Si/Ti molar ratio for most synthesized materials. As the Ti content increased, the specific surface area decreased, whereas the band gap energy increased. The UV-Vis-DRS spectrum showed an absorption band around 230 nm, which is commonly associated with ligand-to-metal charge transfer transitions in isolated Ti species with tetrahedral coordination. Together with the XPS results, these findings suggest that the Ti incorporated into the silica framework is predominantly in tetrahedral coordination. Small amounts of Ti in Ti-SBA-15 materials are sufficient to promote photocatalytic acetaminophen degradation, without requiring significant anatase formation. Catalyst dosage and solution pH significantly influenced system performance, with higher degradation rates observed under acidic conditions. However, the rapid disappearance of acetaminophen did not directly translate into high mineralization, as aromatic intermediates are difficult to break down into carboxylic acids. Consequently, the maximum mineralization achieved was 50%, obtained with a catalyst concentration of 50 mg/L at pH 6. The proposed reaction scheme successfully predicted the experimental data. These results show that the Ti-SBA-15 system possesses a high capacity for degrading acetaminophen; however, complete mineralization is limited by the slow oxidation rate of aromatic intermediates, making the control of subsequent degradation stages a key factor in improving the overall efficiency of the photocatalytic process.

Keywords: acetaminophen; degradation; photocatalysis; SBA-15; Ti-SBA-15

Academic Editor: Óscar Manuel González Díaz

Received: 6 September 2026
Revised: 28 September 2026
Accepted: 5 October 2026
Published: 8 October 2026

Copyright: © 2026 by the authors. Licensee MDPI, Basel, Switzerland. This article is an open access article distributed under the terms and conditions of the Creative Commons Attribution (CC BY) license.

1. Introduction

With population growth and urbanization, the cosmetic, textile, and pharmaceutical industries have significantly increased production. In particular, the synthesis of analgesic and non-steroidal anti-inflammatory drugs (NSAIDs), such as ibuprofen, naproxen, and aspirin, has increased because they effectively relieve pain, inflammation, and fever by inhibiting cyclooxygenase (COX) enzymes. Several studies have reported these pharmaceuticals in wastewater effluents, surface and groundwater, and even in drinking water, generally at concentrations on the order of ng/L or μg/L. Continuous exposure to these emerging contaminants, even at low concentrations, may adversely affect human health and aquatic ecosystems [1,2]. Acetaminophen (APAP), also known as paracetamol ($C_8H_9NO_2$), is one of the most widely used analgesic and antipyretic drugs worldwide because of its high efficacy, low cost, and safety profile when administered at therapeutic doses. Therefore, it is widely recommended for different population groups, including children, older adults, and pregnant women under medical supervision [1,3]. Nevertheless, consumption at high doses is a concern, as it may induce the formation of toxic metabolites, such as N-acetyl-p-benzoquinone imine (NAPQI), which is responsible for hepatic and renal damage. In addition, a fraction of the unmetabolized drug is excreted and released into the environment through wastewater, contributing to the contamination of water bodies and posing ecotoxicological risks [1,3].

In this context, pharmaceuticals such as APAP pose a significant challenge for conventional water treatment systems, which are not designed to remove emerging contaminants efficiently. Processes such as biodegradation, coagulation–flocculation, and filtration have limitations in completely removing these compounds, driving the search for more efficient alternative technologies. Among the most widely studied processes are electrochemical oxidation [4], Fenton processes [5], ozonation [6], persulfate-based oxidation [7] and advanced oxidation processes (AOPs) based on heterogeneous catalysis [8]. The latter have shown increasing potential for degrading organic contaminants in aqueous media because of their high activity, stability, ease of recovery, and ability to mineralize persistent organic contaminants [1,2,9].

Among the catalysts reported in the literature for heterogeneous catalytic advanced oxidation processes are mixed oxides, such as TiO_2/Fe_2O_3, investigated for paracetamol degradation [3]. $ZnO/CeO_2/g\text{-}C_3N_4$ nanocomposites were also used to degrade acetaminophen and caffeine [9].

Catalysts based on liquid gallium metal (GLM), such as Cu/Ga_2O_3, were applied to acetaminophen degradation [10]. In addition, silica-based materials, including SBA-15, were investigated as heterogeneous catalysts for advanced oxidation processes [1,8,11–14].

Various catalysts have been employed for the photodegradation of acetaminophen, among which titanium dioxide (TiO_2) stands out. This material has demonstrated high degradation efficiencies under ultraviolet irradiation, achieving removal percentages greater than 90% in times exceeding 90 min [15]. To improve performance, several studies have investigated doping TiO_2 with different elements, such as carbon [16] and metals including silver, gold, platinum, and iron [17,18].

SBA-15-type mesoporous silicates stand out as highly promising photocatalysts due to their textural and structural properties. This material exhibits large pore diameters that favor diffusion of relatively large pharmaceutical molecules, as well as high specific surface areas (generally exceeding 800 m^2/g) and large pore volumes, enabling efficient adsorption of organic contaminants [1,8,11–14]. Its ordered mesoporous structure with hexagonal symmetry (P6mm) provides thermal and mechanical stability, while also facilitating the incorporation and homogeneous distribution of metallic heteroatoms (Ti, Zn, Ag, among others) within its structure [19,20]. This modification could change the electronic

structure of the material, such as reducing the band gap, thereby favoring radiation absorption and the generation of electron–hole pairs, which are fundamental in photocatalytic processes [21,22].

Several studies have also evaluated SBA-15 as an adsorbent for acetaminophen and have reported contaminant removal percentages exceeding 80% under relatively accessible operating conditions [22–24]. In particular, an optimum pH near 5 and a material dosage of 1 g/L have been identified for treating solutions containing up to 150 mg/L acetaminophen [22].

In photocatalytic processes, SBA-15 is commonly used as a support for metal oxides or other active compounds to impart photocatalytic properties [22–24]. For example, the incorporation of 10-phenylphenothiazine (PTH) into the SBA-15 structure enabled its use in the photodegradation of paracetamol under simulated solar irradiation. Under these conditions, using a catalyst loading of 250 mg/L and an initial paracetamol concentration of 10 mg/L, a conversion of 70% was achieved after 6 h of reaction [24]. Iron-modified SBA-15 materials have also been investigated as catalysts for the degradation of organic contaminants [25,26]. Hernández et al. synthesized Fe-incorporated SBA-15 and achieved degradation close to 84% using 20 mg/L catalyst concentration in the presence of H_2O_2 under ultraviolet irradiation [27]. Other related studies have evaluated the influence of parameters such as Fe content, pH, temperature, the presence of H_2O_2, catalyst concentration, and initial paracetamol concentration [1]. Similarly, other studies have shown that incorporating metals such as Fe, Ni, Cr, and Co into SBA-15 significantly improves catalytic activity while preserving the hexagonal mesoporous structure of the support. Materials with a high specific surface area may also enhance contaminant adsorption due to this textural property [22–24].

Ti-modified SBA-15 materials have shown great potential as photocatalysts for degrading dyes and pharmaceuticals. Several studies have reported the synthesis of Ti-SBA-15 materials with different Si/Ti molar ratios [28,29]. The incorporation of Ti into the SBA-15 structure promotes the formation of surface Ti–OH groups, which can react with photogenerated holes (h^+) to produce hydroxyl radicals (•OH). These radicals are highly oxidizing and drive the degradation of organic contaminants. Likewise, when Ti is well dispersed within SBA-15, it can partially suppress the recombination of photogenerated electron–hole pairs. This increases charge-carrier lifetime and improves the photocatalytic efficiency [28–30].

The incorporation of titanium into the SBA-15 structure and its use in photocatalytic applications are of particular interest because the photocatalytic performance of Ti-SBA-15 materials is enhanced by the presence of Ti–O–Si bonds [28,29,31] and because titanium acts as a photocatalytic center [31,32]. As the Ti content within the SBA-15 structure increases, anatase TiO_2 formation becomes more pronounced, accompanied by decreases in the specific surface area, pore volume, and pore diameter [28,29,31,32].

The preparation of Ti-modified SBA-15 catalysts is complex due to the significant difference between the hydrolysis kinetics of Ti and Si precursors [33], as well as the tendency of metal species to dissociate during hydrothermal treatment under acidic conditions [34,35]. Although synthesis methods generally incorporate titanium after synthesis, this often leads to anatase TiO_2 formation rather than isomorphic substitution of Ti into the silica framework [31,32]. To improve titanium dispersion and substitution within the SBA-15 structure, a few studies have been reported regarding synthesis methods and conditions based on a single-step co-condensation approach [34,35]. This direct synthesis methodology has yielded Ti-SBA-15 materials in which Ti is either isomorphically substituted or dispersed within the SBA-15 framework, thereby increasing the number of active sites, such as Ti–OH and Ti–OH–Si groups [36,37].

A detailed understanding of paracetamol degradation kinetics is another important aspect for the potential design of water treatment systems. Most studies assume kinetics in which the photocatalytic reaction begins immediately upon irradiation; however, under real-world conditions, this does not occur, because contaminant molecules must first adsorb onto the active sites of the catalyst. From this perspective, several authors [2,3,33,34] have proposed analyzing the kinetics using the Langmuir–Hinshelwood model, which incorporates the adsorption equilibrium preceding the surface reaction. While previous studies have identified certain reaction intermediates and proposed simplified degradation pathways, a quantitative kinetic model for acetaminophen degradation using heterogeneous catalysts has not yet been reported in the literature.

In this context, the present study proposes a comprehensive approach to investigating acetaminophen photodegradation using Ti-SBA-15 materials synthesized via a one-step sol–gel process. This method enabled the incorporation of Ti into the SBA-15 structure while allowing the relative proportions of Ti sites to be varied. Unlike studies that focus primarily on crystalline TiO_2 phases, particularly anatase, this work considers the contribution of Ti species incorporated into the SBA-15 framework and their potential role in photocatalytic acetaminophen degradation. Furthermore, the effects of catalyst dosage and solution pH on acetaminophen degradation are systematically evaluated, and a reaction scheme is proposed and fitted to integrate the formation and transformation of the main reaction intermediates identified during the process.

2. Results and Discussion

2.1. Characterization of Materials

2.1.1. X-Ray Diffraction

Figure 1 shows the low-angle X-ray diffraction patterns of SBA-15 and Ti-modified SBA-15. The SBA-15 sample exhibits three well-defined reflections at $2\theta = 0.94$, 1.61, and 1.86°, indexed to the (100), (110), and (200) planes, respectively, characteristic of a two-dimensional hexagonal mesostructure with p6mm symmetry [35]. As Ti is incorporated up to a Si/Ti molar ratio of 10, the diffraction peaks shift toward lower 2θ values, indicating unit-cell expansion (Table 1). This behavior is consistent with isomorphic substitution of Si^{4+} by Ti^{4+} within the silica framework, because Ti has a larger ionic radius (0.72 Å) than Si (0.40 Å), increasing the interplanar spacing and the unit cell parameter (a_0) [36,37]. As the Ti content increases, corresponding to a decrease in the Si/Ti molar ratio to 5, a different trend is observed. The (100) reflection shifts toward higher 2θ values, indicating mesostructure contraction (in accordance with Table 1), likely associated with framework densification induced by the high Ti loading [38]. In addition, the disappearance of the (110) and (200) reflections suggests a significant loss of long-range hexagonal order, likely due to structural distortion and partial disruption of the mesoporous framework at high Ti content [38,39]. The difference in the low-angle X-ray diffraction pattern of Ti(5)-SBA-15 compared with the other materials may be attributed to the relatively high amount of Al species present in the synthesis gel. High Al content may affect interactions between the surfactant and the silica network during mesostructure formation, resulting in a less ordered surfactant–silica mesostructure. This behavior is consistent with the results reported by Xing et al. and Gajardo et al. [40,41].

Table 1. Crystallographic and textural parameters of SBA-15 and Ti-SBA-15 materials.

Material	d_{100} [a] (nm)	a_0 [b] (nm)	S_{BET} [c] (m^2/g)	V_P [d] (cm^3/g)	D_P [e] (nm)	W [f] (nm)
SBA-15	9.39	10.84	830	0.8	5.3	5.5
Ti(60)-SBA-15	10.15	11.72	768	0.8	4.8	6.9
Ti(40)-SBA-15	10.15	11.72	755	0.9	4.9	6.8
Ti(10)-SBA-15	10.38	11.99	591	0.6	4.1	7.8
Ti(5)-SBA-15	7.68	8.86	355	0.5	4.9	3.9

[a] interplanar distance calculated from the (100) plane of the X-ray diffraction patterns; [b] unit cell parameter a_0 calculated through the formula, $a_0 = 2d_{100}/\sqrt{3}$; [c] specific surface area determined by BET method; [d] pore volume; [e] pore diameter determined by BJH method; [f] wall thickness determined through the equation, $W = a_0 - D_{BJH}$.

Figure 2 shows the wide-angle X-ray diffraction patterns of the synthesized materials. The SBA-15 sample exhibits a broad band centered at $2\theta \approx 23°$, characteristic of the amorphous silica framework. After the incorporation of Ti at Si/Ti molar ratios of 60 and 40, the broad signal characteristic of the amorphous structure persists, indicating that Ti incorporation at high Si/Ti molar ratios does not disrupt the amorphous silica framework. The Ti(5)-SBA-15 and Ti(10)-SBA-15 materials exhibit a broad shoulder at 23°, characteristic of SBA-15 materials. They also show diffraction peaks at $2\theta = 25.3°$, 37.9°, 48.0°, 54.3°, and 62.6°, which are assigned to TiO_2 in the anatase phase (PDF 21-1272) [35,36,42]. In contrast, the Ti(5)-SBA-15 sample shows only these anatase-related reflections, indicating that crystalline TiO_2 predominates over the mesostructured silica framework at high Ti loading. These results suggest a limit to Ti incorporation into the SBA-15 framework under the synthesis conditions employed. The absence of anatase reflections in samples with higher Si/Ti ratios does not necessarily rule out the presence of TiO_2; rather, it indicates that Ti species are highly dispersed or present in domains below the XRD detection limit [43].

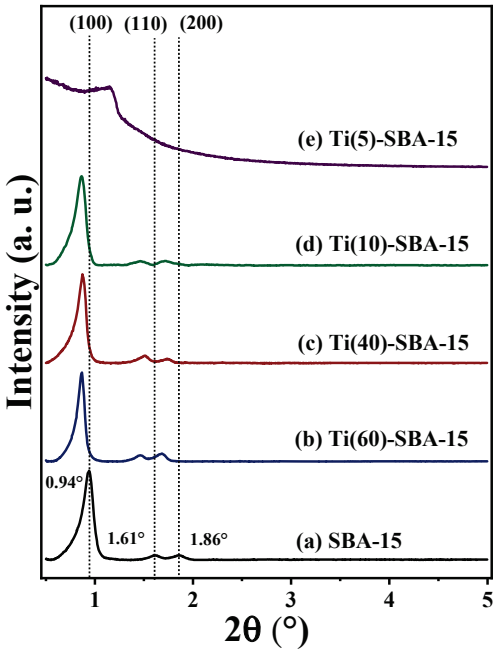


Figure 1. Low-angle X-ray diffraction patterns for SBA-15 and Ti-SBA-15 materials.

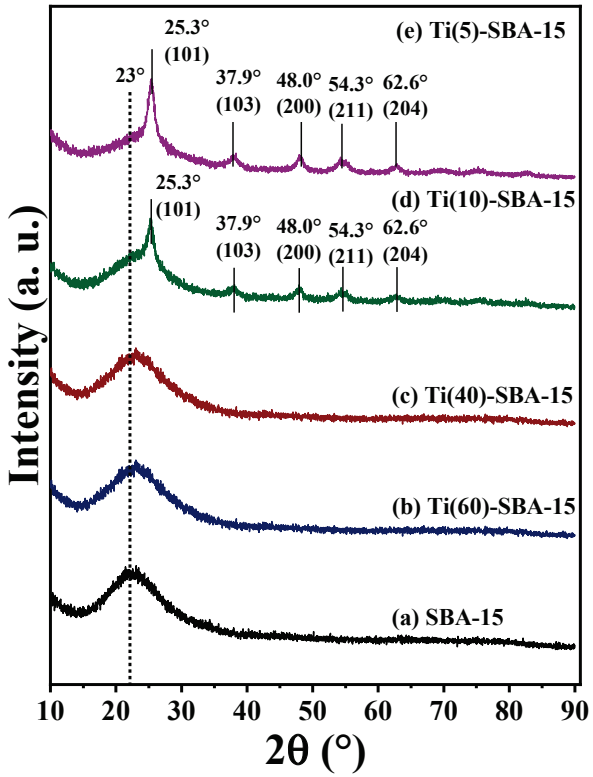


Figure 2. Wide-angle X-ray diffraction patterns for SBA-15 and Ti-SBA-15 materials.

2.1.2. N_2 Physisorption

N_2 adsorption–desorption isotherms of SBA-15 and Ti-SBA-15 materials are shown in Figure 3. All samples exhibit type IV isotherms with H1-type hysteresis loops, characteristic of mesoporous materials with uniform cylindrical pores. The hysteresis loop for SBA-15, Ti(60)-SBA-15, and Ti(40)-SBA-15 materials appears in the relative pressure (P/P_0) range of 0.5–0.75. In contrast, samples with higher Ti loadings, Ti(10)-SBA-15 and Ti(5)-SBA-15, show a slight shift in the hysteresis loop toward lower P/P_0 values, indicating a decrease in pore diameter. This behavior is consistent with the pore diameter distributions obtained by the BJH method (Table 1) and can be attributed to framework contraction, network densification, and partial pore blocking by Ti species, as discussed in Section 3.1.1. Table 1 summarizes the specific surface areas of the synthesized materials. Upon Ti incorporation, surface area decreases, becoming more pronounced at higher Ti loadings (Si/Ti = 5). This reduction is attributed to pore blocking by extra-framework TiO_2 species dispersed within the mesoporous channels [36], consistent with the wide-angle X-ray diffraction results, which confirm that high Ti loading partially disrupts the mesoporous framework.

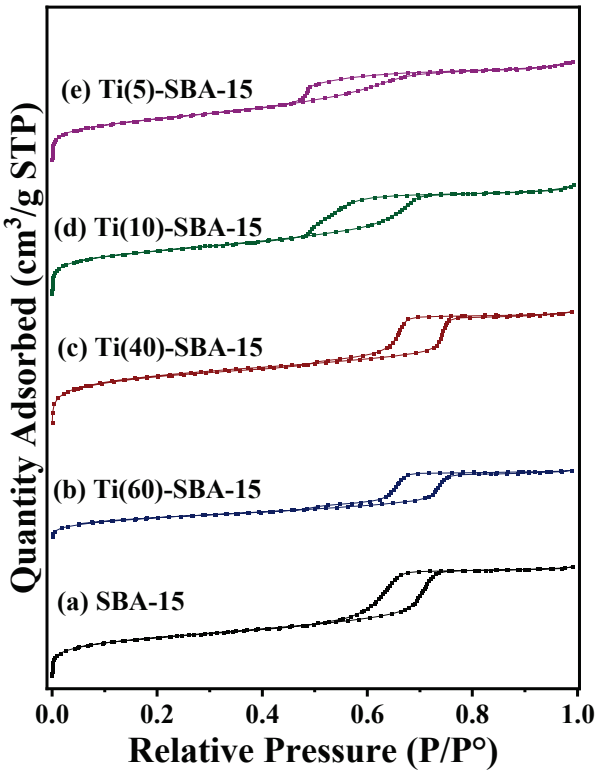


Figure 3. N_2 adsorption–desorption isotherms of SBA-15 and Ti-SBA-15 materials.

2.1.3. Morphology and Elemental Analysis of Synthesized Materials

Figure 4 shows the morphology of SBA-15 and Ti-SBA-15 materials. The SBA-15 sample (Figure 4a) exhibits uniform rod-like particles (152.1 ± 30.6), characteristic of SBA-15 materials. After incorporation Ti (Figure 4b–e), a reduction in particle length accompanied by morphological changes is observed compared to the SBA-15 material (Figure 4a). The particle length of SBA-15 was 152.11 ± 30.59 μm, whereas the Ti-containing materials exhibited progressively smaller particle lengths of 141.85 ± 45.39, 128.40 ± 27.41, 115.20 ± 29.27, and 102.19 ± 27.82 μm for Ti(60)-SBA-15, Ti(40)-SBA-15, Ti(10)-SBA-15, and Ti(5)-SBA-15, respectively. Thus, the particle length decreased by approximately 6.8, 15.6, 24.3, and 32.8% relative to SBA-15 as the Ti content increased. In materials with higher Si/Ti ratios, Ti(60)-SBA-15 and Ti(40)-SBA-15, the particles retain morphologies relatively similar to those of SBA-15, together with moderate reductions in length. In contrast, Ti(10)-SBA-15 and Ti(5)-SBA-15 exhibit more pronounced reductions in particle length and greater morphological differences than the elongated morphology of SBA-15. These differences are particularly evident for Ti(5)-SBA-15 (Figure 4e), which exhibits the largest reduction in particle length among the Ti-containing materials. The progressive morphological changes associated with increasing Ti content may be related to the coexistence of the mesostructured silica phase and TiO_2 species, particularly at lower Si/Ti ratios, as corroborated by the wide-angle X-ray diffraction results discussed in Section 2.1.2. Overall, the SEM results indicate that increasing Ti content is accompanied by a progressive reduction in particle length and modification of particle morphology, with the most pronounced changes observed at the highest Ti loading [44].

Table 2 shows the theoretical and experimental Si/Ti molar ratios of the synthesized materials obtained by ICP–OES analysis. Except for the Ti(60)-SBA-15 sample, the experimental Si/Ti ratios for the remaining materials were relatively close to their theorical values. The experimental Si/Ti molar ratio for Ti(60)-SBA-15 indicates a lower Ti content than

expected based on the theoretical composition. The acidic hydrothermal conditions (pH = 2.5) used during material synthesis may have favored the dissociation of Ti–O–Si bonds, resulting in lower Ti incorporation into the calcined material. Similar deviations between theoretical and experimental Si/Ti ratios have been reported for Ti-SBA-15-50 materials (Si/Ti molar ratio = 50) prepared via a one-step sol–gel hydrothermal method, where such deviations were attributed to the dissociation of Ti–O–Si bonds [45].

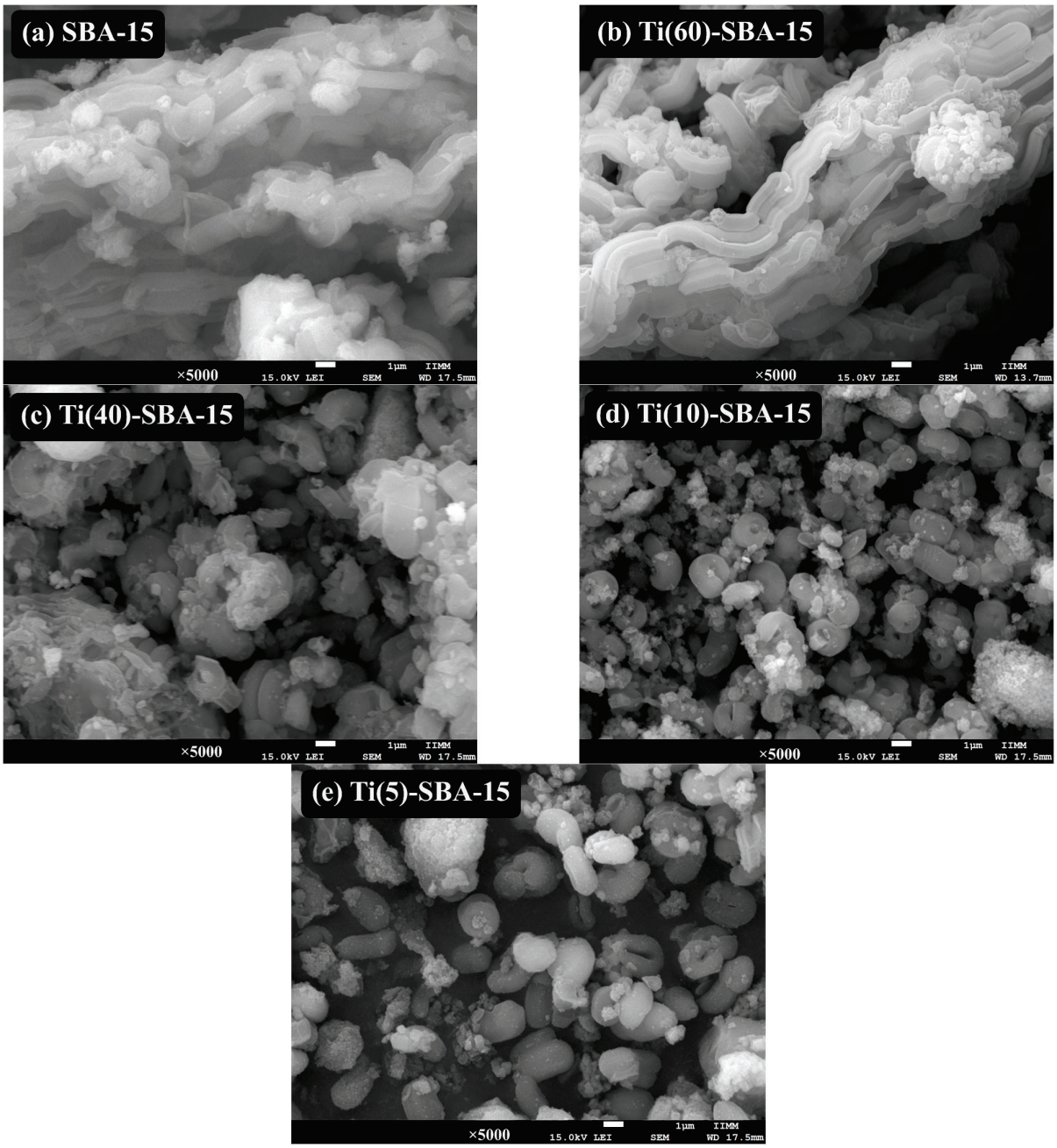


Figure 4. SEM images of (**a**) SBA-15, (**b**) Ti(60)-SBA-15, (**c**) Ti(40)-SBA-15, (**d**) Ti(10)-SBA-15 and (**e**) Ti(5)-SBA-15 materials.

Table 2. Elemental analysis of SBA-15 and Ti-SBA-15 materials determined by ICP-OES.

Material	Theorical Molar Ratio	Experimental Molar Ratio
	Si/Ti	Si/Ti
SBA-15	∞	∞
Ti(60)-SBA-15	60	112
Ti(40)-SBA-15	40	30
Ti(10)-SBA-15	10	12
Ti(5)-SBA-15	5	5

2.1.4. UV–Vis–DRS

Figure 5 presents the UV–Vis spectra of SBA-15 and Ti-SBA-15 materials. The SBA-15 sample shows no significant absorption in the UV–Vis region, confirming the absence of Ti species within the silica framework. The deconvoluted UV–Vis spectrum of the Ti(60)-SBA-15 material exhibits a single absorption band centered at 230 ± 6 nm; this feature is attributed to tetrahedrally coordinated Ti species [46], specifically arising from the ligand-to-metal charge-transfer (LMCT) transition of isolated TiO_4 sites [47]. This suggests that, at low Ti loadings, titanium is predominantly incorporated into the silica framework. These results are consistent with X-ray diffraction and N_2 physisorption analyses.

As the Ti content in the synthesis gel increases, the Ti(40)-SBA-15, Ti(10)-SBA-15, and Ti(5)-SBA-15 materials (Figure 5c–e) exhibit, in addition to the band associated with tetrahedral Ti, a second absorption band at 310 ± 10 nm. This band is commonly attributed to extra-framework Ti species, which may correspond to oligomeric Ti species or anatase-like TiO_2 particles [46,47]. Furthermore, as the Ti loading increases (Table 2), the contribution of extra-framework Ti species becomes more pronounced, in agreement with the X-ray diffraction results.

The band gap energies (Eg) were estimated from the plot of $(\alpha h\nu)^{1/2}$ versus photon energy ($h\nu$) (Figure S1, Supplementary Materials) and are shown in Table 3. As the amount of TiO_2 species in the anatase phase and/or oligomeric Ti, the band gap decreases, approaching the characteristic value of anatase TiO_2 [48]. The band gap values obtained in this study are consistent with those reported in the literature [49]. Anatase TiO_2 exhibits a smaller band gap (3.20 eV) [40] than SBA-15 because its conduction band is mainly composed of lower-energy Ti 3d states strongly hybridized with O 2p orbitals, whereas the conduction band of SBA-15 is primarily associated with higher-energy Si 3p states [50,51]. Therefore, the incorporation of anatase TiO_2 into the SBA-15 framework introduces Ti 3d electronic states within the silica band structure, progressively reducing the effective band gap of the composite toward that of anatase TiO_2 [51].

Table 3. Ti coordination's within the silica network and band gap of the SBA-15 and Ti-SBA-15 materials.

Material	Ti^{4+}	TiO_2	E_g (eV)
SBA-15	0	0	0
Ti(60)-SBA-15	100	0	3.72
Ti(40)-SBA-15	95	5	3.56
Ti(10)-SBA-15	92	8	3.46
Ti(5)-SBA-15	82	18	3.40

Ti^{4+}: Tetrahedral Ti(IV) species; TiO_2: TiO_2 species; E_g: The band gap energy.

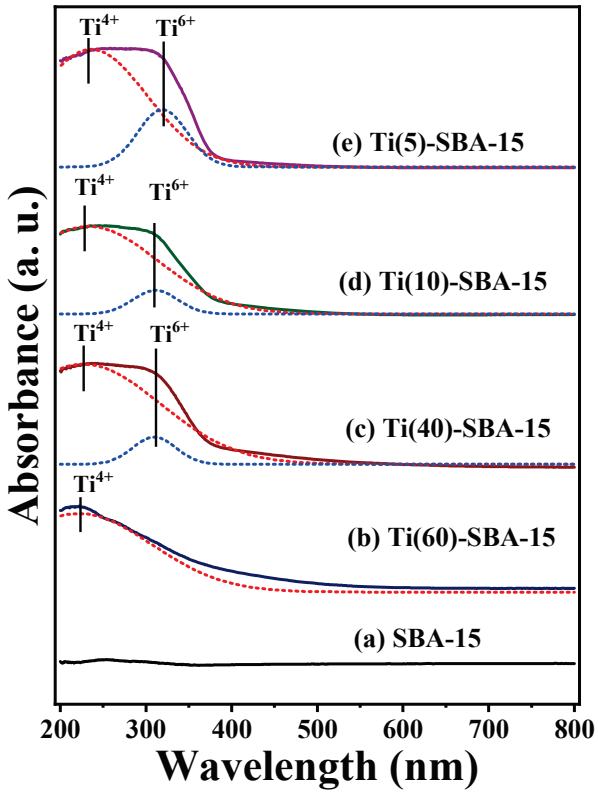


Figure 5. UV-Vis spectra of SBA-15 and Ti-SBA-15 materials. The solid lines correspond to the original spectra, while the dotted lines show the deconvoluted spectra for the Ti^{4+} (red) and Ti^{6+} (blue) species.

2.1.5. XPS

The XPS survey spectra of the synthesized materials are shown in Figure S2. The spectra show characteristic signals of Si 2p (~103 eV), C 1s (~285 eV), and O 1s (~532 eV) [52], while the Ti-containing materials also show the Ti 2p signal at approximately 458–464 eV. The O KLL Auger signal is also observed at approximately 980 eV. The presence of Si 2p and O 1s signals in all samples is consistent with the SBA-15 silica framework. In contrast, the Ti-containing materials show a Ti 2p signal, which is absent in unmodified SBA-15, indicating Ti species at the catalyst surface. The Ti 2p signal becomes more evident as the nominal Ti content increases, corresponding to a decrease in the Si/Ti molar ratio.

Figure 6 shows the Si 2p XPS spectra of the Ti-SBA-15 materials. The SBA-15 spectrum shows a doublet at 100.5 and 103.5 eV, characteristic of tetrahedrally coordinated Si forming Si–O–Si bonds [8,53–55]., confirming successful formation of the mesoporous silica framework. After Ti incorporation into the silica structure, both peaks shift toward lower binding energies, likely due to Ti–O–Si bond formation [56,57]. Because of the electronegativity difference between Ti and Si, these bonds modify the electron-density distribution around the silicon atoms, resulting in the observed shift [56,57]. Furthermore, this shift becomes more pronounced as the amount of Ti incorporated into the material framework increases.

Figure 7 shows the Ti 2p XPS spectra of the Ti-containing materials. The materials with the lowest Ti content (Ti(60)-SBA-15 and Ti(40)-SBA-15) exhibit a doublet located at 458.0 and 463.9 eV, corresponding to the Ti 2p3/2 and Ti 2p1/2, respectively. These binding energies are characteristic of Ti^{4+} species incorporated into the silica framework through Ti–O–Si bonds [27,58], consistent with results from low-angle X-ray diffraction (Section

2.1.1) and UV–Vis diffuse reflectance spectroscopy (UV–Vis DRS) (Section 2.1.4). In contrast, the Ti(10)-SBA-15 and Ti(5)-SBA-15 materials exhibit a slight shift in the Ti 2p3/2 and Ti 2p1/2 doublet toward lower binding energies, suggesting changes in the electronic environment of Ti arising from modifications in the Ti–O–Si bonding [56,58]. Moreover, both materials show an additional peak at binding energies above 464.4 eV, which is attributed to surface TiO_2 species [59–62]. These results are consistent with those obtained by wide-angle X-ray diffraction (Section 2.1.1), where only these materials exhibited the characteristic reflections of the anatase phase. This finding suggests that, when the Ti content exceeds the incorporation capacity of the silica framework, a fraction of the titanium remains as TiO_2 species. Wu et al. [63] suggest that tetrahedral Ti^{4+} species promote ligand-to-metal charge transfer during photocatalytic processes, thereby generating highly active photoexcited charge carriers. These species may facilitate electron–hole pair generation and separation under UV–Vis irradiation.

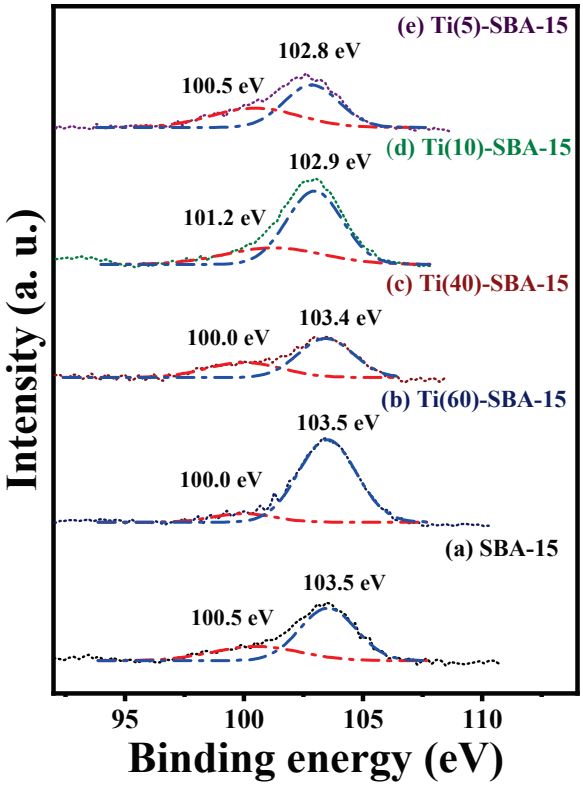


Figure 6. Si 2p XPS spectra of SBA-15 and Ti-SBA-15 materials. The solid lines correspond to the original spectra, while the dotted lines show the deconvoluted spectra for the doublet of Si^{4+}.

Figure 8 displays the high-resolution O 1s XPS spectra of the samples. For the SBA-15 and low Ti loadings, the spectra are fitted into two main components: a feature at ~532–533 eV, attributed to Si–O–Si siloxane bonds in the silica framework [60], and a prominent high-binding-energy peak at ~535 eV, assigned to surface silanol groups (Si–O–H) and/or adsorbed molecular water [60]. Upon increasing the Ti content, particularly for samples with Si/Ti ratio ≤ 10 [Ti(10)–SBA-15 and Ti(5)–SBA-15], a distinct contribution emerges at lower binding energy (~529 eV). This component is characteristic of lattice oxygen (O^{2-}) in extra-framework TiO_2 phases (such as anatase) [38,62], which confirms the agglomeration of TiO_2 species at high titanium loadings, in full agreement with the XRD observations.

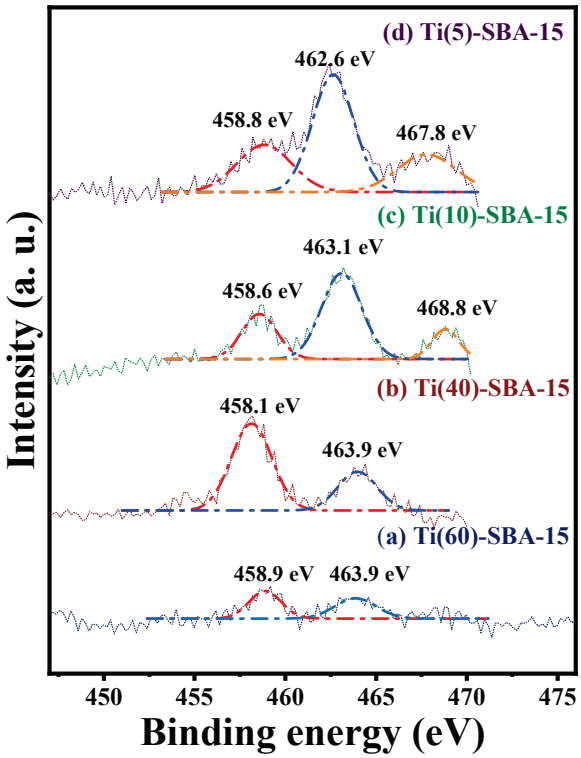


Figure 7. Ti 2p XPS spectra of the Ti-synthesized materials. The dotted lines represent the original spectra, while the blue and red lines correspond to the two components of the Ti^{4+} doublet, and the orange lines correspond to the TiO_2 species.

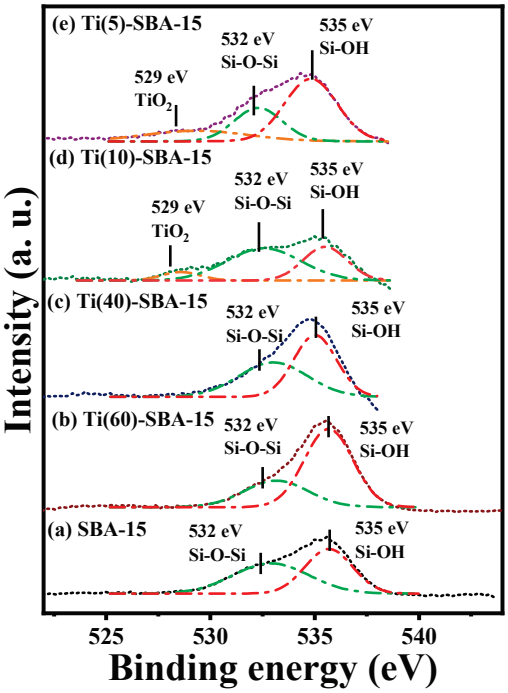


Figure 8. O 1s XPS spectra of SBA-15 and Ti-SBA-15 materials. The solid lines correspond to the original spectra, while the dotted lines show the deconvoluted components assigned to Si–OH (red), Si–O–Si (green), and TiO_2 (orange).

2.1.6. Zeta Potential

Figure 9 presents the zeta potential as a function of pH for the Ti-SBA-15 catalysts. The isoelectric point of SBA-15 was determined to be pH_{IEP} = 1, which is consistent with values reported in the literature) [61]. The SBA-15 surface is predominantly composed of silanol groups (Si–OH), which exhibit acidic behavior and readily undergo deprotonation, thereby generating a negative surface charge over most of the pH range. This characteristic explains why the isoelectric point of the material occurs at low pH values.

The incorporation of titanium into the SBA-15 structure significantly shifts the isoelectric point. The Ti-modified materials exhibited an isoelectric point at pH values close to 5 and 6, characteristic of the anatase phase of TiO_2 ($pH_{IEP} \approx 6$) [61]. Titanium incorporation promotes the formation of Ti–O and Ti–OH bonds, which are less acidic than silanol groups, shifting the isoelectric point toward higher pH values.

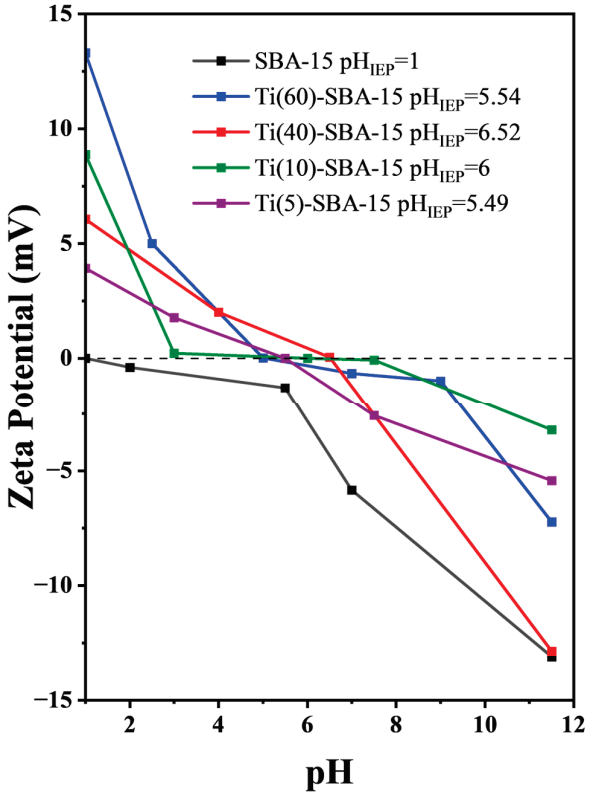


Figure 9. Effect of Ti content of Ti-SBA-15 materials on the isoelectric point.

2.2. Photocatalytic Experiments for the Degradation of Acetaminophen

Figure 10 shows the normalized acetaminophen concentration profiles as a function of time for the different catalysts. This figure includes a dark experiment which was conducted to rule out the contribution of contaminant adsorption on the catalyst surface; the results indicated that such effects were negligible. Likewise, a control experiment without catalyst was performed, in which a 30% degradation was recorded after 240 min, attributable to photolysis. Finally, a photodegradation test using TiO_2 was conducted to compare with the performance of Ti-SBA-15 materials. Based on these results, Ti(5)-SBA-15 and Ti(10)-SBA-15, as well as the titanium-free sample, showed lower degradation than anatase TiO_2, whereas Ti(40)-SBA-15 performed similarly to TiO_2. Meanwhile, Ti(60)-SBA-15 showed improved degradation extent and degradation rate, achieving 99% degradation after 240 min of reaction.

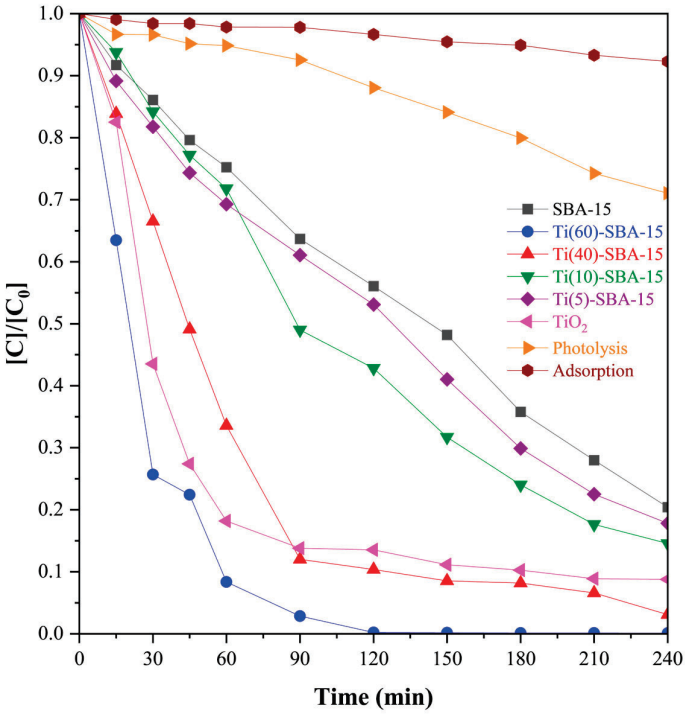


Figure 10. Normalized concentration profiles of acetaminophen for each of the evaluated catalysts. Catalyst loading = 100 mg/L and pH = 6.

2.2.1. Effect of Ti Species in Ti-SBA-15 Materials on the Rate of Acetaminophen Degradation

As shown in Figure 10, the rate of acetaminophen degradation depends on the type of Ti species present in the materials, as well as their Si/Ti molar ratio in Ti-SBA-15 materials. According to the characterization results (UV-Vis), materials with Si/Ti ratios of 60 and 40 show a higher proportion of tetrahedral Ti species incorporated into the SBA-15 framework, whereas Ti oxide or polymeric species are not favored in these materials.

To quantitatively compare the reaction rate for acetaminophen degradation for the different materials synthesized in this study, first-order apparent kinetic constants were calculated based on data in Figure 10 (Figure S3 of the Supplementary Material). As seen in Table 4, the catalysts that convert acetaminophen more rapidly are Ti(60)-SBA-15 and Ti(40)-SBA-15 followed by TiO_2. This indicates that, despite containing significantly less Ti than TiO_2, these materials show comparable conversion rates. As mentioned in the literature, the incorporation of titanium into the SBA-15 structure is of particular interest because the photocatalytic performance of Ti-SBA-15 materials is enhanced by the presence of Ti–O–Si bonds [24] and because titanium acts as a photocatalytic center [29,30]. As the Ti content within the SBA-15 structure increases without modifying the hexagonal arrangement, photocatalytic activity generally increases when Ti is incorporated at Si/Ti molar ratios between 40 and 60. However, when the Si/Ti ratio is below 10, titanium deposits as anatase TiO_2, obstructs SBA-15 pore channels, limits contaminant mass transport, and consequently decreases catalytic performance [29,30]. Therefore, the photocatalytic performance of Ti-SBA-15 materials is governed by a balance between the incorporation of highly dispersed tetrahedral Ti species into the SBA-15 framework, the accessibility and mass transport provided by the porous structure, and the formation of anatase TiO_2 domains at higher Ti contents, with excessive anatase formation becoming detrimental because of its effect on pore accessibility and the subsequent degradation of acetaminophen and its intermediates.

Table 4. Apparent first-order kinetic constant for the synthesized materials.

Material	Apparent First-Order Kinetic Constants (min^{-1})
SBA-15	0.0063
Ti(60)-SBA-15	0.0319
Ti(40)-SBA-15	0.014
Ti(10)-SBA-15	0.0084
Ti(5)-SBA-15	0.0071
TiO_2	0.0096

2.2.2. Effect of Catalyst Content and Solution pH on Acetaminophen Degradation

The effect of catalyst loading (50, 100, and 200 mg/L) and solution pH (3, 6, and 9) on the kinetics of the photocatalytic reaction was investigated using the Ti(60)-SBA-15 material, with three independent experiments performed for each test condition. After 240 min of reaction, the acetaminophen solution exhibited a pronounced chromatic transition: the initial transparency evolved into persistent turbidity upon completion of the process. The evolution of acetaminophen concentration was monitored by UV–Vis spectroscopy. Figure 11 presents the normalized concentration profiles obtained under each experimental condition.

According to the profiles (Figure 11), a catalyst loading of 50 mg/L and pH = 3 enabled 99% degradation in only 30 min. Lower catalyst loadings achieved higher degradation performance. This behavior can be attributed to the increased concentration of catalyst particles in the reaction medium, which enhances light scattering and attenuation, thereby reducing photon penetration and producing a light-shielding effect [64]. In contrast, acidification enhanced degradation efficiency, whereas basic conditions inhibited the process. According to the zeta potential characterization, the Ti(60)-SBA-15 material exhibits an isoelectric point at pH = 5.54; therefore, operation under acidic conditions imparts a net positive surface charge to the solid surface. This electrostatic configuration promotes the chemisorption of water molecules and the subsequent generation of hydroxyl radicals (•OH), thereby increasing the acetaminophen degradation rate.

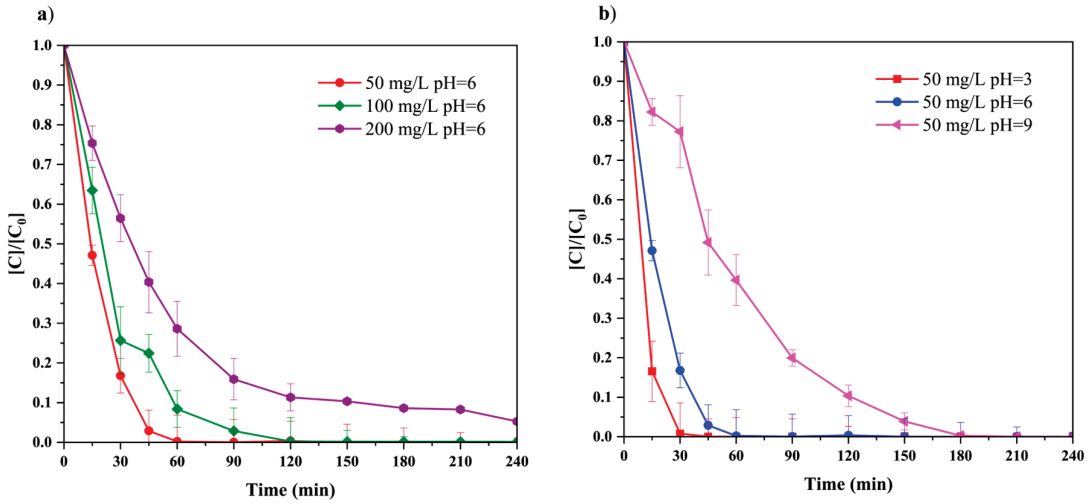


Figure 11. Effect of catalyst loading (**a**) and solution pH (**b**) on the normalized acetaminophen concentration profiles over Ti(60)-SBA-15 catalyst. T = 25 °C and initial acetaminophen concentration = 5 mg/L.

2.2.3. Effect of Solution pH on Acetaminophen Mineralization

The degree of mineralization for the highest-performing catalyst dosage (50 mg/L) at various pH levels was determined through total organic carbon (TOC) analysis (Figure 12). This analysis assumes that the decrease in residual organic carbon concentration is directly proportional to the decomposition of reaction intermediates into inorganic species. Although conditions of 50 mg/L at pH 3 resulted in approximately 99% degradation of acetaminophen within 30 min, the degradation of the parent compound does not necessarily imply complete mineralization, as intermediate oxidation products may remain in the reaction medium. In this regard, the highest degree of mineralization was achieved with the same catalyst concentration but at pH 6, reaching approximately 50%; conversely, under basic conditions, mineralization decreased drastically, likely due to the limited degradation of intermediate compounds into CO_2 and H_2O.

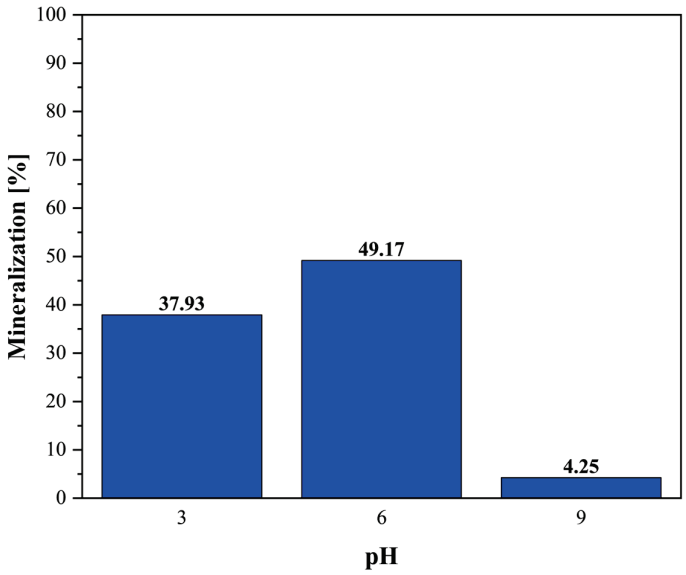


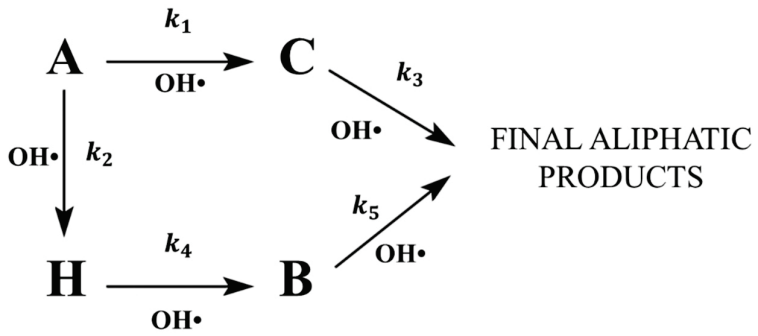
Figure 12. Effect of solution pH on acetaminophen mineralization degree, using the Ti(60)-SBA-15 catalyst with a catalyst dosage of 50 mg/L.

2.2.4. Product Distribution and Reaction Scheme for Acetaminophen Degradation over the Ti(60)-SBA-15 Catalyst

A detailed analysis of the reaction products during acetaminophen degradation experiments using high-performance liquid chromatography allowed us to identify the most important components, including acetaminophen (A), hydroquinone (H) catechol (C), and benzoquinone (B), as well as carboxylic acids such as oxamic acid, oxalic acid, succinic acid, malonic acid, acetic acid and formic acid (see Figure S4, Supplementary Material). In all cases, a rapid production of aromatic compounds was observed, linked to the rapid degradation of acetaminophen; meanwhile, hydroquinone also showed rapid conversion to benzoquinone—which was the most abundant product at the end of the reaction, except under basic conditions, where catechol was the predominant compound. However, both benzoquinone and catechol exhibited stability after a certain period, suggesting they were not degraded into simpler compounds; this aligns with the low formation of carboxylic acids observed in all cases.

Analysis of the reaction products at different times made it possible to identify the main reaction pathways. Due to the partial positive charge density of the acetamido group, this region exhibits greater susceptibility to attack by the hydroxyl radical [2,65]. This process forms aromatic intermediates such as hydroquinone and catechol.

Subsequently, hydroquinone oxidation yields benzoquinone via a reversible redox mechanism that establishes a chemical equilibrium state [66,67]. Finally, successive hydroxylation of the benzene ring promotes its cleavage, leading to the generation of carboxylic acids [3,68]. Based on the foregoing, a reaction scheme for the photodegradation of acetaminophen was proposed, as shown in Scheme 1. From the product distribution, it was observed that the concentration of carboxylic acids was low compared with that of aromatic compounds; therefore, the latter were used to formulate the kinetic model and mass balances (Scheme 1).



Scheme 1. Proposed simplified reaction scheme for the photodegradation of acetaminophen using the Ti(60)-SBA-15 catalyst under ultraviolet light. Acetaminophen (A), Catechol (C), Hydroquinone (H), Benzoquinone (B).

Langmuir–Hinshelwood-type kinetic expressions were proposed (Equations (1)–(5)) for each of the reactions in Scheme 1, and the experimental data were subsequently fitted to the proposed kinetic model [2,3,33,34].

$$r_1 = \frac{k_1 K_A [C_A]}{1 + K_A[C_A] + K_H[C_H] + K_C[C_C] + K_B[C_B]} \quad (1)$$

$$r_2 = \frac{k_2 K_A [C_A]}{1 + K_A[C_A] + K_H[C_H] + K_C[C_C] + K_B[C_B]} \quad (2)$$

$$r_3 = \frac{k_3 K_C [C_C]}{1 + K_A[C_A] + K_H[C_H] + K_C[C_C] + K_B[C_B]} \quad (3)$$

$$r_4 = \frac{k_4 K_H [C_H]}{1 + K_A[C_A] + K_H[C_H] + K_C[C_C] + K_B[C_B]} \quad (4)$$

$$r_5 = \frac{k_5 K_B [C_B]}{1 + K_A[C_A] + K_H[C_H] + K_C[C_C] + K_B[C_B]} \quad (5)$$

Based on the stated reaction expressions, component balances were performed, which are given by (Equations (6)–(9)):

$$\frac{dC_A}{dt} = -r_1 - r_2 \quad (6)$$

$$\frac{dC_C}{dt} = r_1 - r_3 \quad (7)$$

$$\frac{dC_H}{dt} = r_2 - r_4 \quad (8)$$

$$\frac{dC_B}{dt} = r_4 - r_5 \quad (9)$$

Kinetic parameters were calculated using a genetic algorithm in MATLAB R2024a, using a system of ordinary differential equations. Kinetic and adsorption constants were estimated via nonlinear least-squares regression based on experimental concentrations of acetaminophen, hydroquinone, catechol, and benzoquinone. The fitting was performed simultaneously for all four species, minimizing the difference between experimental data and model predictions. Figure 13 shows the product distribution for the most representative experiments.

Figure 13 shows that acetaminophen degradation proceeds rapidly, accompanied by the formation of aromatic intermediates. In contrast, the aromatic compounds remained stable after approximately 60 min of reaction. The model fit the experimental data well, as evidenced by the deviation of the experimental data; however, it fit hydroquinone less well under pH 3 and pH 6 conditions.

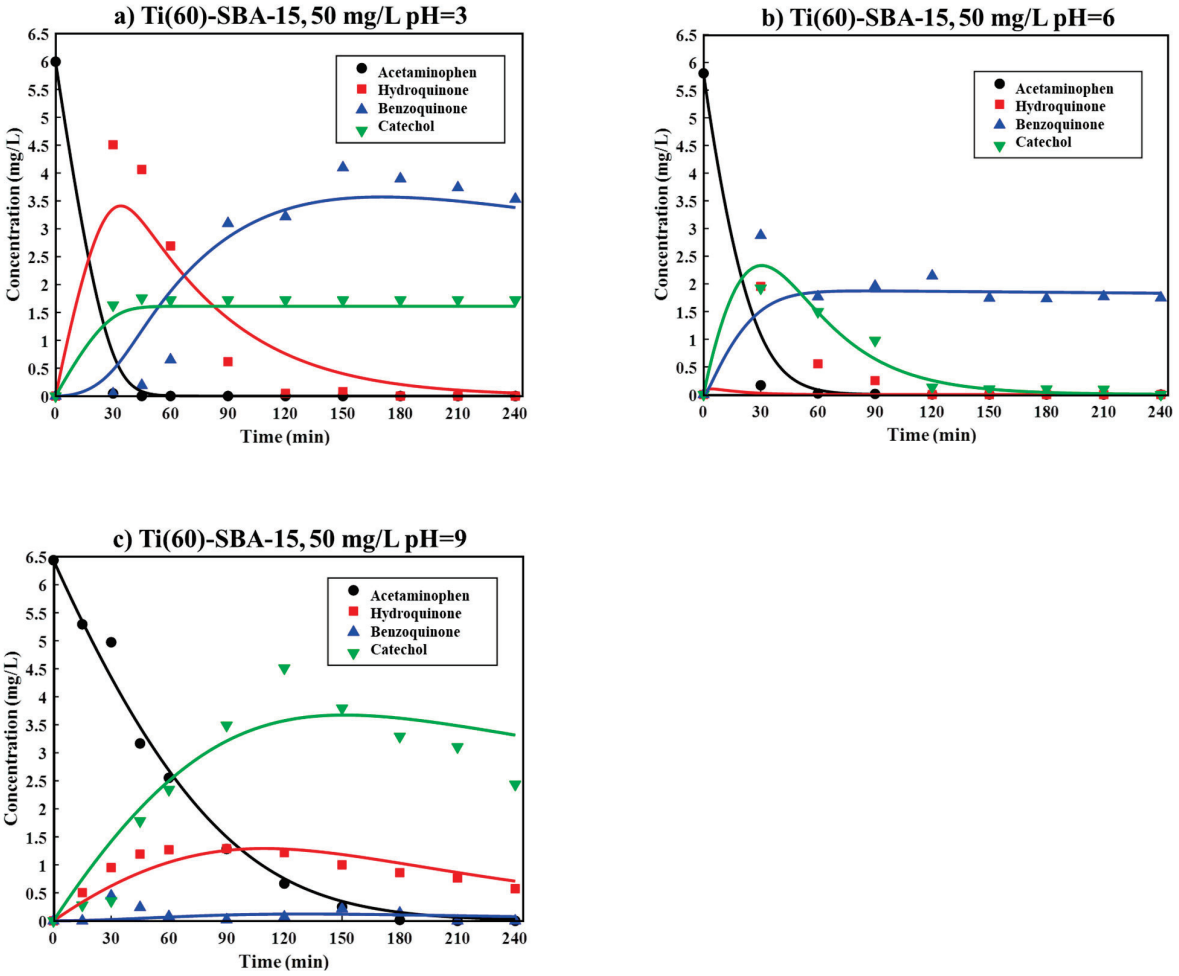


Figure 13. Fitting of the proposed kinetic model for the photodegradation of acetaminophen using the Ti(60)-SBA-15 catalyst under different experimental conditions. The experimental data are represented by points, while the solid line corresponds to the fit.

The distribution of data around the parity line (Figure 14) demonstrates a good correspondence between the two sets of values, yielding a coefficient of determination of $R^2 = 0.93$. This result indicates that the model can reproduce the concentration profiles of the compounds involved in the degradation process, thereby supporting the validity of the proposed kinetic scheme.

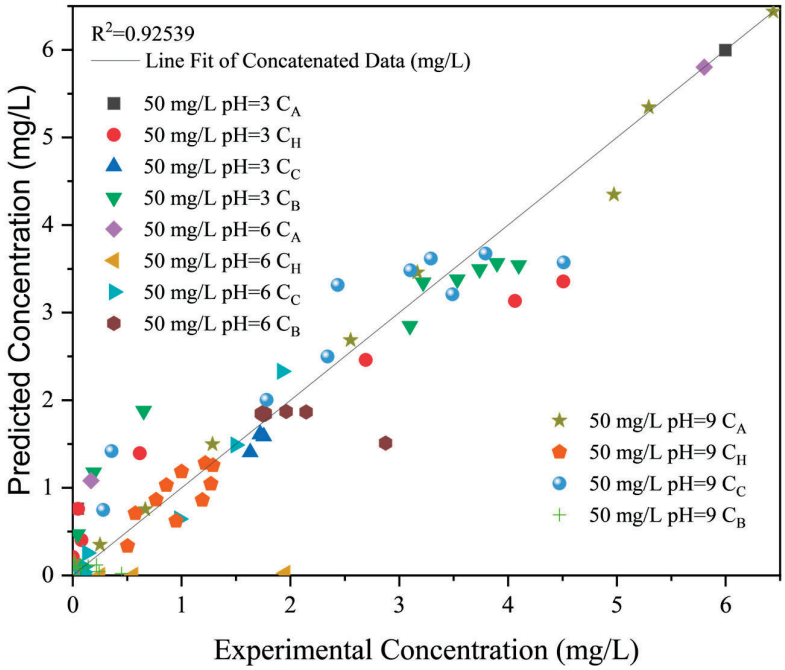


Figure 14. Parity plot for experimental and calculated concentrations for acetaminophen, hydroquinone, catechol, and benzoquinone.

Tables 5 and 6 present the kinetic and adsorption constants obtained by fitting the experimental data to the proposed reaction model. The results indicate that the predominant reaction pathways depend on the experimental conditions employed. For example, at pH = 6, the rate constants associated with intermediate transformation are particularly favorable, which aligns with the higher degree of mineralization observed. Conversely, at acidic pH, a rapid kinetic constant for the formation of hydroquinone and catechol is observed; however, the consumption of both is much lower than at pH 6. This suggests that acetaminophen disappears rapidly without necessarily implying extensive oxidation; consequently, the main limitation of the process appears to lie not in the initial transformation of acetaminophen, but in the subsequent stages of oxidation and aromatic ring opening, consistent with the low concentration of carboxylic acids detected experimentally.

Table 5. Values of the kinetic constants estimated from fitting the kinetic model to experimental data.

Experimental Condition	Kinetic Constants (mg L^{-1} min^{-1})				
	k_1	k_2	k_3	k_4	k_5
50 mg/L pH = 3	0.088	1.006	0.036	0.172	0.033
50 mg/L pH = 6	0.480	0.337	0.431	1.713	0.214
50 mg/L pH = 9	0.136	0.210	0.655	0.317	0.134

Table 6. Values of the adsorption constants estimated from fitting the kinetic model to experimental data.

Experimental Condition	Adsorption Constants (L mg^{-1})			
	K_A	K_H	K_C	K_B
50 mg/L pH = 3	0.530	0.159	5.18×10^{-5}	0.059
50 mg/L pH = 6	0.125	0.936	0.074	0.001
50 mg/L pH = 9	0.118	0.116	0.001	0.061

https://doi.org/10.3390/catal16100892

3. Materials and Methods

3.1. Catalyst Synthesis

3.1.1. Synthesis of SBA-15 Material

The SBA-15 support was synthesized by dissolving 3.3 g of Pluronic P123 (Sigma-Aldrich, St. Louis, MO, USA) in a 0.2 M HCl solution containing 1.8 g of NaCl (Sigma-Aldrich, St. Louis, MO, USA; purity ≥ 99.0%). After 2 h of stirring, 6.9 mL of tetraethyl orthosilicate (TEOS) (Sigma-Aldrich, St. Louis, MO, USA; purity ≥ 99.0%) was added, and the mixture was stirred at 40 °C for 24 h. The resulting gel was transferred to a hydrothermal reactor and aged at 100 °C for 24 h. The solid was recovered by filtration, washed with deionized water to neutral pH, and dried at 80 °C overnight. The material was calcined in air at 550 °C using a heating rate of 1 °C min^{-1} for 6 h [69].

3.1.2. Synthesis of Ti-SBA-15 Material

Ti-modified SBA-15 was synthesized by dissolving 3.3 g of Pluronic P123 (Sigma-Aldrich) in a 0.2 M HCl solution containing 1.8 g of NaCl. After 2 h of stirring, 6.9 mL of tetraethyl orthosilicate (TEOS) was added, and the mixture was stirred at 40 °C for 2 h. The Titanium precursor, titanium isopropoxide (Sigma-Aldrich, St. Louis, MO, USA; purity = 97.0%), was then introduced in varying amounts (0.15, 0.22, 0.89, and 1.77 mL for an Si/Ti molar ratio of 60, 40, 10, and 5, respectively). The resulting gel was aged at 40 °C for 24 h, then transferred to a hydrothermal reactor and aged at 100 °C for 24 h. The solid was recovered by filtration, washed with deionized water to neutral pH, and dried at 80 °C overnight. The material was calcined in air at 550 °C using a heating rate of 1 °C min^{-1} for 6 h [69].

3.2. Characterization of Catalysts

X-ray diffraction (XRD) patterns were recorded on a Bruker D8 Advance diffractometer (Madison, WI, USA) operating in low-angle mode over a 2θ range of 0.5–5°. Data were collected using a step size of 0.0048° and a counting time of 0.2 s per step. The instrument had primary and secondary slits of 0.2 and 5 mm, respectively, and a LynxEye detector (Karlsruhe, Germany) with a 1° aperture. Measurements were performed using Cu Kα radiation at 40 kV and 30 mA. N_2 adsorption–desorption isotherms were measured at 77 K using a TriStar II 3020 analyzer (Micromeritics - Norcross, GA, USA). The specific surface area was calculated by the Brunauer–Emmett–Teller (BET) method. Pore diameter distribution and pore volume were determined from the desorption branch of the isotherms using the Barrett–Joyner–Halenda (BJH) method. Prior to analysis, the samples were degassed at 150 °C for 24 h. Scanning electron microscopy (SEM) images were obtained using a JEOL JSM-7600F microscope (Tokyo, Japan) operated under high vacuum at an accelerating voltage of 30 kV and a magnification of 5000×. Prior to analysis, the samples were sputter-coated with a conductive layer to prevent charging. Elemental analysis was performed by inductively coupled plasma optical emission spectrometry (ICP–OES) using a Vista MPX simultaneous instrument (Varian - Varian, Mulgrave, Victoria, Australia). Prior to analysis, the samples were digested in a mixture of concentrated HNO_3, HCl, and HF (1:1:1, *v*/*v*/*v*) for 24 h. An aliquot of the digest (1 mL) was diluted to a final volume of 50 mL with deionized water prior to measurement. UV–vis diffuse reflectance spectra (DRS) were recorded at room temperature over 200–800 nm range using a Lambda 35 spectrophotometer (PerkinElmer - Shelton, CT, USA) equipped with an integrating sphere. Prior to analysis, the samples were finely ground to obtain homogeneous powders. X-ray photoelectron spectroscopy (XPS) was used to determine the elemental composition and chemical states of the materials. Survey spectra were acquired over a binding energy range of 50–1000 eV, and high-resolution spectra were recorded for the

core levels of the elements using a JPS-9200 spectrometer (JEOL - Tokyo, Japan). The binding energy scale was calibrated by setting the C 1s peak of adventitious carbon to 285 eV. A Shirley-type background was applied to all high-resolution spectra, and peak areas were used for quantification. To determine the isoelectric point of the material, the zeta potential was measured as a function of solution pH using a Brookhaven particle size and zeta potential analyzer, operated at 110–240 V and 50–60 Hz. The pH of the aqueous suspensions (1 mg L^{-1}) was adjusted by adding 10% *v*/*v* HNO_3 and 0.7 N NaOH.

3.3. Photocatalytic Test

To evaluate the photoactivity of the material in acetaminophen degradation, 100 mL of an aqueous solution with an initial concentration of 5 mg/L was used without prior pH adjustment. The catalyst loading was 100 mg/L. After identifying the catalyst with the highest degradation efficiency, the influence of operational variables such as catalyst concentration and solution pH were studied. To analyze the effect of catalyst loading, three concentrations were tested: 50, 100, and 200 mg/L. To examine the influence of initial solution pH, we adjusted the pH to 3, 6, and 9 using 10% *v*/*v* nitric acid and 0.1 N sodium hydroxide, as appropriate.

The photocatalytic reaction was conducted in a 200 mL cylindrical reactor equipped with a cooling system and operated at 750 rpm. After adding the required amount of catalyst, the mixture was kept in the dark for 15 min to ensure adsorption–desorption equilibrium. Next, a 254 nm mercury ultraviolet lamp (UV PEN-Ray Light Source 11SC-2.12 P/N 90-010012-01 (UVP/Analytik Jena, USA), with a radiation intensity of 1500–2000 μW/cm^2 and 5 W) was switched on, positioned directly in the reactor at a distance of 10 cm from the suspension, and the system was irradiated for 4 h. Aliquots of 2 mL were collected at the beginning of the process and at 0, 15, 30, 45, 60, 90, 120, 150, 180, 210, and 240 min.

The residual acetaminophen concentration as a function of time was determined by UV–Vis spectroscopy at 243 nm, corresponding to the maximum absorption of the molecule.

Additionally, high-performance liquid chromatography was employed to identify the intermediate degradation products using a UHPLC Vanquish system (Thermo Scientific, Waltham, MA, USA), and the degree of mineralization was determined by measuring total organic carbon with a Shimadzu TOC Analyzer.

For the identification of reaction products, high-performance liquid chromatography was used on a UHPLC Vanquish Thermo Scient Scientific instrument, where the following columns and mobile phases were used according to the type of compound to be analyzed:

- Acetaminophen: Acclaim 120 C18 column, with Water:Methanol 70:30 as mobile phase.
- Aromatic compounds: Ascentis Express C18 column, with Water:Methanol 80:20/213 μL H_2SO_4 96% as mobile phase.
- Carboxylic acids: Bio-Rad Aminex HPX-87H column, with 100% 3 mM H_2SO_4 as mobile phase.

4. Conclusions

The one-step hydrothermal sol–gel method enabled the incorporation of Ti at different Si/Ti molar ratios into the SBA-15 structure, with values close to the theoretical ones. Incorporation of relatively high Ti contents in SBA-15 (Si/Ti = 5 and 10) induced a contraction and loss of the hexagonal P6mm arrangement of SBA-15, accompanied by the appearance of a crystalline phase corresponding to anatase TiO_2. On the other hand, when Ti is

incorporated in small amounts (Si/Ti = 40 and 60), the UV–Vis-DRS and XPS results revealed that Ti was predominantly incorporated in tetrahedral coordination (Ti^{4+}) through the formation of Ti–O–Si bonds within the SBA-15 silica framework. As the titanium loading increased, the band-gap energy decreased, while the amount of Ti species associated with anatase TiO_2 on the catalyst surface increased.

The substitution of Si by Ti in the SBA-15 materials modified the surface chemistry of the material. Zeta potential measurements suggested that Ti–O bonds and Ti–OH groups shifted the isoelectric point from pH_{IEP} = 1 for the silica framework to values near pH_{IEP} = 5.5–6.5. This change promoted a net positive surface charge under acidic conditions, improving the adsorption/chemisorption of water molecules and hydroxyl groups (OH^-), which are key to the generation of free radicals (•OH) in photocatalysis.

Incorporating small amounts of Ti into the SBA-15 structure significantly improved the photocatalytic degradation of acetaminophen, suggesting that low Ti levels suffice to promote photocatalytic activity without requiring significant anatase phase formation; this finding is linked to the mass transport of paracetamol within the channels of the SBA-15 structure. Tetrahedral Ti species appear to catalyze the initial degradation stages of the parent molecule, as shown in Figure 10; however, mineralization results (Figure 12) and product distribution (Figure 13) indicate that these species do not catalyze extensive degradation. Furthermore, at low Ti concentrations, only tetrahedral Ti species form, favoring rapid acetaminophen degradation, whereas increasing the Ti content can promote anatase formation and potentially obstruct reactant access. Consequently, various factors may limit acetaminophen mineralization in this system.

Furthermore, catalyst dosage and solution pH significantly influenced system performance, with higher degradation rates observed under acidic conditions. The results indicate that acetaminophen removal and mineralization did not proceed at the same rate, since the aromatic intermediates generated during photocatalysis exhibited greater resistance to further oxidation toward carboxylic acids. Under the evaluated conditions, the highest mineralization level was 50%, achieved at a catalyst concentration of 50 mg/L and pH 6. In addition, the proposed reaction scheme provided a satisfactory representation of the experimental behavior and accurately predicting the measured concentration profiles. Overall, the Ti-SBA-15 system demonstrated a strong ability to promote acetaminophen degradation, whereas the progressive oxidation of the resulting aromatic compounds remained the main limitation to complete mineralization. Therefore, improving the efficiency of these subsequent reaction steps is essential for enhancing the overall performance of the photocatalytic process.

Supplementary Materials: The following supporting information can be downloaded at: https://www.mdpi.com/article/10.3390/catal16100892/s1, Figure S1. Determination of the bandgap of a) Ti(60)-SBA-15; b) Ti(40)-SBA-15; c) Ti(10)-SBA-15; d) Ti(5)-SBA-15 materials.; Figure S2. XPS survey spectrum of SBA-15 and Ti-SBA-15 materials.; Figure S3. Calculation of first-order apparent kinetic constants for the Ti-SBA-15 catalysts; Figure S4. Product distribution for the photodegradation of acetaminophen (aromatic compounds and carboxylic acids) over Ti(60)-SBA-15 catalysts under different pH and catalyst loadings.

Author Contributions: Conceptualization, J.P.C.-L., M.L.L.-G., J.E.-V. and H.G.; methodology, J.P.C.-L., M.L.L.-G., D.A.S.-C., U.C.-F. and D.A.-P.; software, J.P.C.-L. and M.L.L.-G.; validation, J.P.C.-L., M.L.L.-G., U.C.-F., D.A.S.-C., J.E.-V., D.A.-P. and H.G.; formal analysis, J.P.C.-L., M.L.L.-G. and H. G.; investigation, J.P.C.-L., M.L.L.-G. and H.G.; resources, H.G., U.C.-F. and J.E.-V.; data curation, J.P.C.-L., M.L.L.-G. and H.G.; writing—original draft preparation, J.P.C.-L. and M.L.L.-G.; writing—review and editing, J.P.C.-L., M.L.L.-G. and H.G.; visualization, J.P.C.-L., M.L.L.-G. and H.G.; supervision, J.P.C.-L., M.L.L.-G., J.E.-V. and H.G.; project administration, J.E.-V. and H.G.;

funding acquisition, J.E.-V. and H.G. All authors have read and agreed to the published version of the manuscript.

Funding: H.G. thanks CIC-UMSNH for its financial support through projects ID: 17017 and 19698. This research was funded by PAPIIT through Projects IV100124 and IN116424.

Data Availability Statement: The original contributions presented in this study are included in the article/supplementary material. Further inquiries can be directed to the corresponding author(s).

Acknowledgments: JPCL and MLLG thank SECIHTI for the scholarships, 820050 and 4023948, respectively. The authors would like to thank P. Casillas, D. Dominguez, and C. Gonzalez for technical assistance.

Conflicts of Interest: The authors declare no conflicts of interest. The funders had no role in the design of the study; in the collection, analyses, or interpretation of data; in the writing of the manuscript; or in the decision to publish the results.

Abbreviations

The following abbreviations are used in this manuscript:

Ti(X)-SBA-15	Material SBA-15 with a Si/Ti molar relation of X value
XRD	X-ray diffraction
SEM	Scanning electron microscopy
ICP-OES	Inductively coupled plasma optical emission spectrometry
UV-Vis-DRS	UV–vis diffuse reflectance spectra
XPS	X-ray photoelectron spectroscopy
N_2	Nitrogen
NSAIDs	Non-steroidal anti-inflammatory drugs
COX	Cyclooxygenase
NAPQI	N-acetyl-p-benzoquinone imine
AOPs	Advanced oxidation processes
GLM	Liquid gallium metal
•OH	Hydroxyl radicals
h^+	Holes
TEOS	Tetraethyl orthosilicate
TOC	Total organic carbon
d_{100}	Interplanar distance
a_0	Cell parameter
S_{BET}	Specific surface area
V_P	Pore volumen
D_P	Pore diameter
W	Wall thickness
LMCT	Ligand-to-metal charge-transfer
Eg	Band gap energies
pH_{IEP}	Isoelectric point
A	Acetaminophen
H	Hydroquinone
C	Catechol
B	Benzoquinone
k_i	Kinetic constant of reaction i
K_A	Acetaminophen adsorption constant
K_H	Hydroquinone adsorption constant
K_C	Catechol adsorption constant
K_B	Benzoquinone adsorption constant
r_i	Reaction rate for the reaction i

References

1. Castro-Campoy, D.A.; Vargas-Hernández, D.; Sánchez-Cruz, M.; Hernández-Huesca, R. Photodegradation of Acetaminophen and Ibuprofen in Iron Supported in SBA-15 under UV Irradiation. *J. Photochem. Photobiol. Chem.* **2023**, *441*, 114716. https://doi.org/10.1016/j.jphotochem.2023.114716.
2. Nasr, O.; Mohamed, O.; Al-Shirbini, A.-S.; Abdel-Wahab, A.-M. Photocatalytic Degradation of Acetaminophen over Ag, Au and Pt Loaded TiO2 Using Solar Light. *J. Photochem. Photobiol. Chem.* **2019**, *374*, 185–193. https://doi.org/10.1016/j.jphotochem.2019.01.032.
3. Abdel-Wahab, A.-M.; Al-Shirbini, A.-S.; Mohamed, O.; Nasr, O. Photocatalytic Degradation of Paracetamol over Magnetic Flower-like TiO2/Fe2O3 Core-Shell Nanostructures. *J. Photochem. Photobiol. Chem.* **2017**, *347*, 186–198. https://doi.org/10.1016/j.jphotochem.2017.07.030.
4. Zhang, Q.; Zhou, Y.; Yu, Y.; Chen, B.-Y.; Hong, J. Exploring Catalytic Performance of Boron-Doped Graphene Electrode for Electrochemical Degradation of Acetaminophen. *Appl. Surf. Sci.* **2020**, *508*, 145111. https://doi.org/10.1016/j.apsusc.2019.145111.
5. Deng, Y.; Zhao, R. Advanced Oxidation Processes (AOPs) in Wastewater Treatment. *Curr. Pollut. Rep.* **2015**, *1*, 167–176. https://doi.org/10.1007/s40726-015-0015-z.
6. Kanakaraju, D.; Glass, B.D.; Goh, P.S. Advanced Oxidation Process-Mediated Removal of Pharmaceuticals from Water: A Review of Recent Advances. *Environ. Sci. Pollut. Res.* **2025**, *32*, 14316–14350. https://doi.org/10.1007/s11356-025-36547-5.
7. Tan, C.; Gao, N.; Deng, Y.; An, N.; Deng, J. Heat-Activated Persulfate Oxidation of Diuron in Water. *Chem. Eng. J.* **2012**, *203*, 294–300. https://doi.org/10.1016/j.cej.2012.07.005.
8. Domínguez-Talamantes, D.G.; Rodríguez-Castellón, E.; Tánori-Córdova, J.C.; García-Bórquez, A.; Ovando-Martínez, M.; Molina-Domínguez, C.C.; Gámez-Meza, N.; Vargas-Hernández, D. Photocatalytic Activity of Metallic Silver Supported on SBA-15 for the Degradation of Methyl Orange and Methylene Blue. *Environ. Sci. Pollut. Res.* **2026**, *33*, 2668–2687. https://doi.org/10.1007/s11356-026-37453-0.
9. Chebwogen, J.; Nyongesa, F.W.; Mwabora, J.M.; Ndungu, P.G. Simultaneous Photodegradation of Acetaminophen and Caffeine Using a ZnO/CeO2/g-C3N4 Nanocomposite. *Discov. Appl. Sci.* **2025**, *7*, 1274. https://doi.org/10.1007/s42452-025-07598-7.
10. Orozco, S.; Valencia, J.E.; Rivero, M. Effect of Copper Salt on the Synthesis of Copper-Doped Gallium Metal Liquid Based Photocatalyst (Cu/Ga2O3), and Its Application in Acetaminophen Photodegradation. *Catal. Commun.* **2023**, *183*, 106779. https://doi.org/10.1016/j.catcom.2023.106779.
11. Bai, L.; Wang, S.; Wang, Z.; Hong, E.; Wang, Y.; Xia, C.; Wang, B. Kinetics and Mechanism of Photocatalytic Degradation of Methyl Orange in Water by Mesoporous Nd-TiO2-SBA-15 Nanocatalyst. *Environ. Pollut.* **2019**, *248*, 516–525. https://doi.org/10.1016/j.envpol.2019.02.052.
12. Zhou, Y. Synthesis, Characterization, and Photo-Catalytic Activity of Ag/ZnO/SBA-15 Composite. *Desalination Water Treat.* **2019**, *159*, 250–256. https://doi.org/10.5004/dwt.2019.24116.
13. Lv, F.; Miao, Y.; Yang, D.; Mao, B.; Bian, Z.; Zhu, F. In Situ Etching Synthesis of TiO2-SBA-15 Nanocomposite Enhancing Adsorption and Photocatalytic Degradation. *Catalysts* **2022**, *12*, 1334. https://doi.org/10.3390/catal12111334.
14. Chawraba, K.; Hamieh, M.; Medlej, H.; Lalevée, J.; Hamieh, T.; Toufaily, J. Advancing Sustainable Photocatalysis: Methylene Blue-Loaded SBA-15 for Efficient Pollutant Degradation under Visible LED Light. *Results Surf. Interfaces* **2025**, *21*, 100651. https://doi.org/10.1016/j.rsurfi.2025.100651.
15. Zhang, X.; Wu, F.; Wu, X.; Chen, P.; Deng, N. Photodegradation of Acetaminophen in TiO2 Suspended Solution. *J. Hazard. Mater.* **2008**, *157*, 300–307. https://doi.org/10.1016/j.jhazmat.2007.12.098.
16. Shaban, Y.A.; Fallata, H.M. Sunlight-Induced Photocatalytic Degradation of Acetaminophen over Efficient Carbon Doped TiO2 (CTiO2) Nanoparticles. *Res. Chem. Intermed.* **2019**, *45*, 2529–2547. https://doi.org/10.1007/s11164-019-03750-2.
17. Aguilar, C.A.; Montalvo, C.; Zermeño, B.B.; Cerón, R.M.; Cerón, J.G.; Anguebes, F.; Ramírez, M.A. Photocatalytic Degradation of Acetaminophen, Tergitol and Nonylphenol with Catalysts TiO2/Ag under UV and Vis Light. *Int. J. Environ. Sci. Technol.* **2019**, *16*, 843–852. https://doi.org/10.1007/s13762-018-1707-x.
18. Peñas-Garzón, M.; Gómez-Avilés, A.; Bedia, J.; Rodriguez, J.J.; Belver, C. Effect of Activating Agent on the Properties of TiO2/Activated Carbon Heterostructures for Solar Photocatalytic Degradation of Acetaminophen. *Materials* **2019**, *12*, 378. https://doi.org/10.3390/ma12030378.
19. Khanh Nguyen, Q.N.; Yen, N.T.; Hau, N.D.; Tran, H.L. Synthesis and Characterization of Mesoporous Silica SBA-15 and ZnO/SBA-15 Photocatalytic Materials from the Ash of Brickyards. *J. Chem.* **2020**, *2020*, 1–8. https://doi.org/10.1155/2020/8456194.

20. Phanikrishna Sharma, M.V.; Durga Kumari, V.; Subrahmanyam, M. TiO2 Supported over SBA-15: An Efficient Photocatalyst for the Pesticide Degradation Using Solar Light. *Chemosphere* **2008**, *73*, 1562–1569. https://doi.org/10.1016/j.chemosphere.2008.07.081.
21. Kim, Y.; Bae, J.; Park, J.; Suh, J.; Lee, S.; Park, H.; Choi, H. Removal of 12 Selected Pharmaceuticals by Granular Mesoporous Silica SBA-15 in Aqueous Phase. *Chem. Eng. J.* **2014**, *256*, 475–485. https://doi.org/10.1016/j.cej.2014.06.100.
22. Natarajan, R.; Venkataraman, S.; Rajendran, D.S.; Tamilselvam, B.; Zaveri, H.; Jeyachandran, N.; Prashar, H.; Vaidyanathan, V.K. Adsorption Performance of Magnetic Mesoporous Silica Microsphere Support toward the Remediation of Acetaminophen from Aqueous Solution. *J. Water Process Eng.* **2022**, *48*, 102835. https://doi.org/10.1016/j.jwpe.2022.102835.
23. Yuan, S.; Wang, M.; Liu, J.; Guo, B. Recent Advances of SBA-15-Based Composites as the Heterogeneous Catalysts in Water Decontamination: A Mini-Review. *J. Environ. Manage.* **2020**, *254*, 109787. https://doi.org/10.1016/j.jenvman.2019.109787.
24. González-Muñoz, D.; Gómez-Avilés, A.; Molina, C.B.; Bedia, J.; Belver, C.; Alemán, J.; Cabrera, S. Anchoring of 10-Phenylphenothiazine to Mesoporous Silica Materials: A Water Compatible Organic Photocatalyst for the Degradation of Pollutants. *J. Mater. Sci. Technol.* **2022**, *103*, 134–143. https://doi.org/10.1016/j.jmst.2021.07.004.
25. Benzaquén, T.B.; Ochoa Rodriguez, P.A.; Cánepa, A.L.; Casuscelli, S.G.; Elías, V.R.; Eimer, G.A. Heterogeneous Fenton Reaction for the Treatment of ACE in Residual Waters of Pharmacological Origin Using Fe-SBA-15 Nanocomposites. *Mol. Catal.* **2020**, *481*, 110239. https://doi.org/10.1016/j.mcat.2018.11.010.
26. Pires, J.; Borges, S.; Carvalho, A.; Pereira, C.; Pereira, A.M.; Fernandes, C.; Araújo, J.P.; Freire, C. Magnetically Recyclable Mesoporous Iron Oxide–Silica Materials for the Degradation of Acetaminophen in Water under Mild Conditions. *Polyhedron* **2016**, *106*, 125–131. https://doi.org/10.1016/j.poly.2016.01.007.
27. Hernández-Oloño, J.T.; Vargas-Hernández, D.; Castro-Campoy, D.A.; Ibarra-Espinoza, A.; Pérez-Cruz, M.A.; Garrafa-Gálvez, H.E.; Herrera-Urbina, J.R.; Tánori-Córdova, J.C. Photo-Catalytic Activity of Iron Nanoparticles Supported on SBA-15 for Degradation of Organic Pollutants. *J. Photochem. Photobiol. Chem.* **2025**, *469*, 116597. https://doi.org/10.1016/j.jphotochem.2025.116597.
28. Elías, V.R.; Ferrero, G.O.; Oliveira, R.G.; Eimer, G.A. Improved Stability in SBA-15 Mesoporous Materials as Catalysts for Photo-Degradation Processes. *Microporous Mesoporous Mater.* **2016**, *236*, 218–227. https://doi.org/10.1016/j.micromeso.2016.09.001.
29. Göl, S.; Akbay, E. The Effect of Metal-Titania Interaction on Photodegradation in SBA-15-Supported Metal-Titania Photocatalysts. *Chem. Ind. Chem. Eng. Q.* **2023**, *29*, 281–289. https://doi.org/10.2298/CICEQ221017001G.
30. Jung, W.Y.; Baek, S.H.; Yang, J.S.; Lim, K.-T.; Lee, M.S.; Lee, G.-D.; Park, S.S.; Hong, S.-S. Synthesis of Ti-Containing SBA-15 Materials and Studies on Their Photocatalytic Decomposition of Orange II. *Catal. Today* **2008**, *131*, 437–443. https://doi.org/10.1016/j.cattod.2007.10.072.
31. Yang, L.; Jiang, Z.; Lai, S.; Jiang, C.; Zhong, H. Synthesis of Titanium Containing SBA-15 and Its Application for Photocatalytic Degradation of Phenol. *Int. J. Chem. Eng.* **2014**, *2014*, 1–7. https://doi.org/10.1155/2014/691562.
32. Zhang, H.; Tang, C.; Lv, Y.; Gao, F.; Dong, L. Direct Synthesis of Ti-SBA-15 in the Self-Generated Acidic Environment and Its Photodegradation of Rhodamine B. *J. Porous Mater.* **2014**, *21*, 63–70. https://doi.org/10.1007/s10934-013-9748-5.
33. Han, Y.; Kim, H.; Park, J.; Lee, S.; Kim, J. Influence of Ti Doping Level on Hydrogen Adsorption of Mesoporous Ti-SBA-15 Materials Prepared by Direct Synthesis. *Int. J. Hydrog. Energy* **2012**, *37*, 14240–14247. https://doi.org/10.1016/j.ijhydene.2012.07.030.
34. Charan, P.H.K.; Rao, G.R. Textural and Morphological Studies of Transition Metal Doped SBA-15 by Co-Condensation Method. *J. Chem. Sci.* **2015**, *127*, 909–919. https://doi.org/10.1007/s12039-015-0847-5.
35. Chen, S.; Ma, C.; Qin, M.; Yang, H.; Xie, H.; Guan, J. Direct Synthesis and Catalytic Activity of Ordered Large Pore Titanium-Substituted Spherical SBA-15 Molecular Sieves. *React. Kinet. Mech. Catal.* **2012**, *106*, 245–256. https://doi.org/10.1007/s11144-012-0426-4.
36. Nghia, N.V.; Vinh, H.X.; Trung, N.T.; Hung, N.P. Synthesis and Characterisation of Nanostructured TiO2/SBA-15 and Ag-TiO2/SBA-15 Mesoporous Composites. *Int. J. Nanotechnol.* **2015**, *12*, 475. https://doi.org/10.1504/IJNT.2015.067905.
37. Wang, X.; Li, F.; Hao, Y.; Liu, S.; Yang, M. TiO2/SBA-15 Composites Prepared Using H2TiO3 by Hydrothermal Method and Its Photocatalytic Activity. *Mater. Lett.* **2013**, *99*, 38–41. https://doi.org/10.1016/j.matlet.2013.02.060.
38. Li, G.; Zhao, X.S. Characterization and Photocatalytic Properties of Titanium-Containing Mesoporous SBA-15. *Ind. Eng. Chem. Res.* **2006**, *45*, 3569–3573. https://doi.org/10.1021/ie0514253.
39. Palanichamy, K.; Sasirekha, N. Dry Reforming of Methane Using Bimetallic Pt–Ni/Ti-SBA-15: Effect of Si/Ti Ratio on Catalytic Activity and Stability. *Int. J. Hydrog. Energy* **2023**, *48*, 31126–31141. https://doi.org/10.1016/j.ijhydene.2023.04.183.
40. Xing, S.; Lv, P.; Fu, J.; Wang, J.; Fan, P.; Yang, L.; Yuan, Z. Direct Synthesis and Characterization of Pore-Broadened Al-SBA-15. *Microporous Mesoporous Mater.* **2017**, *239*, 316–327. https://doi.org/10.1016/j.micromeso.2016.10.018.

41. Gajardo, J.; Colmenares-Zerpa, J.; Peixoto, A.F.; Silva, D.S.A.; Silva, J.A.; Gispert-Guirado, F.; Llorca, J.; Urquieta-Gonzalez, E.A.; Santos, J.B.O.; Szanyi, J.; Sepúlveda, C.; Álvarez, M. G.; Chimentão, R. J. Revealing the effects of high Al loading incorporation in the SBA-15 silica mesoporous material. *J. Porous Mater*. **2023**, 30(5). 1687–1707. https://doi.org/10.1007/s10934-023-01453-z
42. Hernández-Perez, I.; Maubert, A.M.; Rendón, L.; Santiago, P.; Herrera-Hernández, H.; Arceo, L.D.-B.; Febles, V.G.; González, E.P.; González-Reyes, L. Ultrasonic Synthesis: Structural, Optical and Electrical Correlation of TiO2 Nanoparticles. *Int. J. Electrochem. Sci.* **2012**, *7*, 8832–8847. https://doi.org/10.1016/S1452-3981(23)18035-7.
43. Pham, X.N.; Nguyen, M.B.; Doan, H.V. Direct Synthesis of Highly Ordered Ti-Containing Al-SBA-15 Mesostructured Catalysts from Natural Halloysite and Its Photocatalytic Activity for Oxidative Desulfurization of Dibenzothiophene. *Adv. Powder Technol.* **2020**, *31*, 3351–3360. https://doi.org/10.1016/j.apt.2020.06.028.
44. Galacho, C.; Ribeiro Carrott, M.M.L.; Valerio, J.; Carrott, P.J.M.; Valente Nabais, J.M. Structural Characterisation and Mechanical Stability of Titanium Substituted Mesoporous Materials. *Mater. Sci. Forum* **2010**, *636*, 136–141. https://doi.org/10.4028/www.scientific.net/MSF.636-637.136.
45. Awoke, Y.; Chebude, Y.; Díaz, I. Controlling Particle Morphology and Pore Size in the Synthesis of Ordered Mesoporous Materials. *Molecules* **2020**, *25*, 4909. https://doi.org/10.3390/molecules25214909.
46. Lu, Q.; Tang, Z.; Zhang, Y.; Zhu, X. Catalytic Upgrading of Biomass Fast Pyrolysis Vapors with Pd/SBA-15 Catalysts. *Ind. Eng. Chem. Res.* **2010**, *49*, 2573–2580. https://doi.org/10.1021/ie901198s.
47. Díez-Rodríguez, T.M.; Blázquez-Blázquez, E.; Lourenço, J.P.; Martínez, J.C.; Cerrada, M.L.; Pérez, E. Preparation and Characterization of Santa Barbara Amorphous-15 Particles Functionalized with Mercaptopropyl Groups and of Their Composites with Poly(Lactic Acid). *Microporous Mesoporous Mater.* **2025**, *382*, 113391. https://doi.org/10.1016/j.micromeso.2024.113391.
48. Guntida, A.; Maugé, F.; Kouvatas, C.; Aguilera, L.-J.; Lebedev, O.I.; Praserthdam, P.; Praserthdam, S.; Thomas, K. Generation of Isolated Ti4+ Sites via One-Pot Synthesis of Mesoporous Ti-SBA-15 Catalysts for High-Performance Oxidative Desulfurization of Dibenzothiophene. *Mater. Today Sustain.* **2025**, *31*, 101204. https://doi.org/10.1016/j.mtsust.2025.101204.
49. Mo, S.; Guo, Y.; Liu, X.; Wang, Y. Efficient Depolymerization of PET over Ti-Doped SBA-15 with Abundant Lewis Acid Sites *via* Glycolysis. *Catal. Sci. Technol.* **2023**, *13*, 6561–6569. https://doi.org/10.1039/D3CY01127E.
50. Bérubé, F.; Kleitz, F.; Kaliaguine, S. A Comprehensive Study of Titanium-Substituted SBA-15 Mesoporous Materials Prepared by Direct Synthesis. *J. Phys. Chem. C* **2008**, *112*, 14403–14411. https://doi.org/10.1021/jp803853m.
51. Besançon, M.; Michelin, L.; Josien, L.; Vidal, L.; Assaker, K.; Bonne, M.; Lebeau, B.; Blin, J.-L. Influence of the Porous Texture of SBA-15 Mesoporous Silica on the Anatase Formation in TiO_2 –SiO_2 Nanocomposites. *New J. Chem.* **2016**, *40*, 4386–4397. https://doi.org/10.1039/C5NJ02859K.
52. Ma, J.; Chu, J.; Qiang, L.; Xue, J. Effect of Different Calcination Temperatures on the Structural and Photocatalytic Performance of Bi-TiO_2 /SBA-15. *Int. J. Photoenergy* **2013**, *2013*, 1–10. https://doi.org/10.1155/2013/875456.
53. Lachheb, H.; Ahmed, O.; Houas, A.; Nogier, J.P. Photocatalytic Activity of TiO2–SBA-15 under UV and Visible Light. *J. Photochem. Photobiol. Chem.* **2011**, *226*, 1–8. https://doi.org/10.1016/j.jphotochem.2011.09.017.
54. Soussi, A.; Ait Hssi, A.; Boujnah, M.; Boulkadat, L.; Abouabassi, K.; Asbayou, A.; Elfanaoui, A.; Markazi, R.; Ihlal, A.; Bouabid, K. Electronic and Optical Properties of TiO2 Thin Films: Combined Experimental and Theoretical Study. *J. Electron. Mater.* **2021**, *50*, 4497–4510. https://doi.org/10.1007/s11664-021-08976-8.
55. Araújo, M.M.; Silva, L.K.R.; Sczancoski, J.C.; Orlandi, M.O.; Longo, E.; Santos, A.G.D.; Sá, J.L.S.; Santos, R.S.; Luz, G.E.; Cavalcante, L.S. Anatase TiO2 Nanocrystals Anchored at inside of SBA-15 Mesopores and Their Optical Behavior. *Appl. Surf. Sci.* **2016**, *389*, 1137–1147. https://doi.org/10.1016/j.apsusc.2016.08.018.
56. Parlett, C.M.A.; Durndell, L.J.; Machado, A.; Cibin, G.; Bruce, D.W.; Hondow, N.S.; Wilson, K.; Lee, A.F. Alumina-Grafted SBA-15 as a High Performance Support for Pd-Catalysed Cinnamyl Alcohol Selective Oxidation. *Catal. Today* **2014**, *229*, 46–55. https://doi.org/10.1016/j.cattod.2013.11.056.
57. Vargas-Hernández, D.; Rubio-Caballero, J.M.; Santamaría-González, J.; Moreno-Tost, R.; Mérida-Robles, J.M.; Pérez-Cruz, M.A.; Jiménez-López, A.; Hernández-Huesca, R.; Maireles-Torres, P. Furfuryl Alcohol from Furfural Hydrogenation over Copper Supported on SBA-15 Silica Catalysts. *J. Mol. Catal. Chem.* **2014**, *383*, 106–113. https://doi.org/10.1016/j.molcata.2013.11.034.
58. Vasconcelos, H.C.; Meirelles, M.; Özmenteş, R. XPS Investigation of Sol–Gel Bioactive Glass Synthesized with Geothermal Water. *Surfaces* **2025**, *8*, 50. https://doi.org/10.3390/surfaces8030050.
59. Chávez-León, J.P.; González, H.; Solís-Casados, D.A.; Navarro-Santos, P.; Caudillo-Flores, U. Investigating the Role of Brönsted and Lewis Acid Sites on the Esterification of Levulinic Acid over Ti–Al–SBA-15 Bifunctional Catalysts. *Ind. Eng. Chem. Res.* **2026**, *65*, 11362–11377. https://doi.org/10.1021/acs.iecr.6c01657.

60. Simonsen, M.E.; Sønderby, C.; Li, Z.; Søgaard, E.G. XPS and FT-IR Investigation of Silicate Polymers. *J. Mater. Sci.* **2009**, *44*, 2079–2088. https://doi.org/10.1007/s10853-009-3270-9.
61. Visuvamithiran, P.; Shanthi, K.; Palanichamy, M.; Murugesan, V. Direct Synthesis of Mn-Ti-SBA-15 Catalyst for the Oxidation of Ethylbenzene. *Catal. Sci. Technol.* **2013**, *3*, 2340. https://doi.org/10.1039/c3cy00306j.
62. Konatu, R.T.; Domingues, D.D.; França, R.; Alves, A.P.R. XPS Characterization of TiO2 Nanotubes Growth on the Surface of the Ti15Zr15Mo Alloy for Biomedical Applications. *J. Funct. Biomater.* **2023**, *14*, 353. https://doi.org/10.3390/jfb14070353.
63. Wu, C.-M.; Peng, R.; Dimitrijevic, N.M.; Rajh, T.; Koodali, R.T. Preparation of TiO2–SiO2 Aperiodic Mesoporous Materials with Controllable Formation of Tetrahedrally Coordinated Ti4+ Ions and Their Performance for Photocatalytic Hydrogen Production. *Int. J. Hydrog. Energy* **2014**, *39*, 127–136. https://doi.org/10.1016/j.ijhydene.2013.10.079.
64. Paiu, M.; Lutic, D.; Favier, L.; Gavrilescu, M. Heterogeneous Photocatalysis for Advanced Water Treatment: Materials, Mechanisms, Reactor Configurations, and Emerging Applications. *Appl. Sci.* **2025**, *15*, 5681. https://doi.org/10.3390/app15105681.
65. Mu, R.; Ao, Y.; Wu, T.; Wang, C.; Wang, P. Synthesis of Novel Ternary Heterogeneous Anatase-TiO2 (B) Biphase Nanowires/Bi4O5I2 Composite Photocatalysts for the Highly Efficient Degradation of Acetaminophen under Visible Light Irradiation. *J. Hazard. Mater.* **2020**, *382*, 121083. https://doi.org/10.1016/j.jhazmat.2019.121083.
66. Qin, W.; Wang, Y.; Fang, G.; Wu, T.; Liu, C.; Zhou, D. Evidence for the Generation of Reactive Oxygen Species from Hydroquinone and Benzoquinone: Roles in Arsenite Oxidation. *Chemosphere* **2016**, *150*, 71–78. https://doi.org/10.1016/j.chemosphere.2016.01.119.
67. Sobczyński, A.; Duczmal, Ł.; Dobosz, A. Photocatalysis by Illuminated Titania:Oxidation of Hydroquinone and p-Benzoquinone. *Monatshefte Chem. Chem. Mon.* **1999**, *130*, 377–384. https://doi.org/10.1007/PL00010219.
68. Palos-Barba, V.; Mendoza, R.N.; Millán-Malo, B.M.; Aguilar-Franco, M.; Peza-Ledesma, C.; Rivera-Muñoz, E.M. SBA-15 with Short-Sized Channels Modified with Fe2O3 Nanoparticles. A Novel Approximation of an Efficient Adsorbent for As Removal in Contaminated Water. *J. Porous Mater.* **2024**, *31*, 1387–1400. https://doi.org/10.1007/s10934-024-01589-6.
69. Cabrera-Munguia, D.A.; González, H.; Tututi-Ríos, E.; Gutiérrez-Alejandre, A.; Rico, J.L. Acid Properties of M-SBA-15 and M-SBA-15-SO_3 H (M = Al, Ti) Materials and Their Role on Esterification of Oleic Acid. *J. Mater. Res.* **2018**, *33*, 3634–3645. https://doi.org/10.1557/jmr.2018.374.

Disclaimer/Publisher's Note: The statements, opinions and data contained in all publications are solely those of the individual author(s) and contributor(s) and not of MDPI and/or the editor(s). MDPI and/or the editor(s) disclaim responsibility for any injury to people or property resulting from any ideas, methods, instructions or products referred to in the content.